

The extended interacting wind structure of Eta Carinae[★]

T. R. Gull,^{1†} K. E. Nielsen,^{1,2} M. F. Corcoran,^{3,4} T. I. Madura,⁵ S. P. Owocki,⁵
C. M. P. Russell,⁵ D. J. Hillier,⁶ K. Hamaguchi,^{3,7} G. V. Kober,^{1,2} K. Weis,⁸ O. Stahl⁹
and A. T. Okazaki¹⁰

¹*Astrophysics Science Division, Code 667, NASA Goddard Space Flight Center, Greenbelt, MD 20771, USA*

²*Department of Physics, IACS, Catholic University of America, Washington DC 20064, USA*

³*CRESST and X-ray Astrophysics Laboratory, Code 662, NASA Goddard Space Flight Center, Greenbelt, MD 20771, USA*

⁴*Universities Space Research Association, 10211 Wincopin Circle, Suite 500, Columbia, MD 20706, USA*

⁵*Bartol Research Institute, University of Delaware, Newark, DE 19716, USA*

⁶*Department of Physics and Astronomy, University of Pittsburgh, Pittsburgh, PA 15260, USA*

⁷*Department of Physics, University of Maryland, Baltimore County, 1000 Hilltop Circle, Baltimore, MD 21250, USA*

⁸*Astronomisches Institut, Ruhr-Universität Bochum, Universitätsstrasse 150, D-44780 Bochum, Germany*

⁹*ZAH, Landessternwarte Heidelberg-Königstuhl, D-69117 Heidelberg, Germany*

¹⁰*Faculty of Engineering, Hokkai-Gakuen University, Toyohira-ku, Sapporo 062-8605, Japan*

Accepted 2009 March 24. Received 2009 February 21; in original form 2008 December 23

ABSTRACT

The highly eccentric binary system, η Car, provides clues to the transition of massive stars from hydrogen-burning via the CNO cycle to a helium-burning evolutionary state. The fast-moving wind of η Car B creates a cavity in η Car A's slower, but more massive, stellar wind, providing an *in situ* probe. The *Hubble Space Telescope*/Space Telescope Imaging Spectrograph (*HST*/STIS), with its high spatial and spectral resolutions, is well matched to follow temporal spatial and velocity variations of multiple wind features. We use observations obtained across 1998–2004 to produce a rudimentary three-dimensional model of the wind interaction in the η Car system. Broad (± 500 km s^{−1}) [Fe II] emission line structures extend 0.7 arcsec (~ 1600 au) from the stellar core. In contrast, [Fe III], [Ar III], [Ne III] and [S III] lines extend only 0.3 arcsec (700 au) from NE to SW and are blue shifted from -500 to $+200$ km s^{−1}. All observed spectral features vary with the 5.54-year orbital period. The highly ionized, forbidden emission disappears during the low state, associated with periastron passage. The high-ionization emission originates in the outer wind interaction region that is directly excited by the far-ultraviolet radiation from η Car B. The *HST*/STIS spectra reveal a time-varying, distorted paraboloidal structure, caused by the interaction of the massive stellar winds. The model and observations are consistent with the orbital plane aligned with the skirt of the Homunculus. However, the axis of the distorted paraboloid, relative to the major axis of the binary orbit, is shifted in a prograde rotation along the plane, which projected on the sky is from NE to NW.

Key words: binaries: spectroscopic – stars: individual: Eta Carinae – stars: winds, outflows.

1 INTRODUCTION

Eta Carinae (η Car) and its ejecta comprise an astrophysical laboratory that allows astronomers to study a massive interacting binary at the beginning of the senior phase in its life cycle. In the 1840s, observers saw a major brightening of η Car that lasted for almost two decades. Today, we see the ejecta of that event, the massive Homunculus ($> 10 M_{\odot}$; Smith 2006), a bipolar reflection nebula expanding outwards at ~ 500 km s^{−1} with a thin, expanding skirt located between its lobes. A less dramatic event in the 1890s led to the ejection of the Little Homunculus, an ionized, bipolar structure ($\sim 0.5 M_{\odot}$) internal to the Homunculus expanding at a few hundred

[★]Based on observations made with the National Aeronautics and Space Agency/European Space Agency (NASA/ESA) *HST*. Support for Programme numbers 7302, 8036, 8483, 8619, 9083, 9337, 9420, 9973, 10957 and 11273 was provided by NASA directly to the Space Telescope Imaging Spectrograph Science Team and through grants from the Space Telescope Science Institute (STScI), which is operated by the Association of Universities for Research in Astronomy, Incorporated, under NASA contract NAS5-26555. Based on observations made with European Southern Observatory telescopes at the La Silla or Paranal Observatories under programme IDs 070.D-0607, 071.D-0168, 074.D-0141, 077.D-0618 and 380.D-0036.

†E-mail: theodore.r.gull@nasa.gov

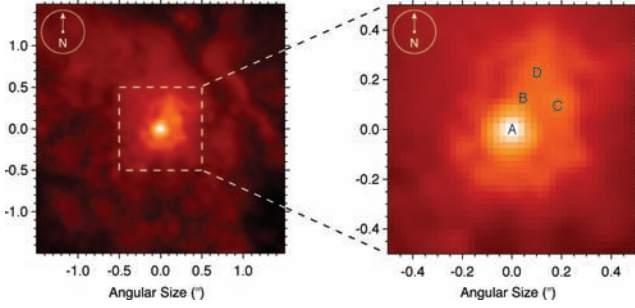


Figure 1. Left-hand panel: central 3-arcsec core of η Car and the Homunculus (*HST*/ACS F555M image). Right-hand panel: central 1 arcsec indicating η Car and the Weigelt condensations. Besides the bright Weigelt condensations (labelled as B, C and D) with intense narrow-line emission, additional condensations appear to form a ring around the central stellar component at a 0.25-arcsec radius. However, spectra of these condensations as seen by *HST*/STIS indicate scattered starlight and extended wind. This entire, complex region contributes to the spatially extended wind which *HST*/STIS resolves, but ground-based, visible spectroscopy cannot.

km s^{-1} (Ishibashi et al. 2003). The Weigelt condensations (Weigelt & Ebersberger 1986), located within 0.2 to 0.3 arcsec of η Car (see Fig. 1), also date back to the 1890s.

At the core of the ejecta is a stellar source with an integrated flux corresponding to $5 \times 10^6 L_{\odot}$, implying a mass exceeding $100 M_{\odot}$. Variations in $\text{He I } \lambda 10830$, which have a periodicity similar to the infrared (IR) and X-ray fluxes (Whitelock et al. 1994; Corcoran 2005), suggested that η Car is a binary system (Damineli 1996). Pittard & Corcoran (2002) fitted wind-shock models to η Car's X-ray spectrum, recorded near apastron, and concluded that the spectrum was formed in the interaction zone between the massive wind of a primary star (η Car A: $\dot{M} \sim 3 \times 10^{-4} M_{\odot} \text{ yr}^{-1}$; $v_{\infty} = 500 \text{ km s}^{-1}$) and the wind of its companion (η Car B: $\dot{M} \sim 1 \times 10^{-5} M_{\odot} \text{ yr}^{-1}$; $v_{\infty} = 3000 \text{ km s}^{-1}$). Recently, Damineli et al. (2008) summarized available multispectral data and demonstrated that slow changes in ionization of the circumstellar material occur across the extended high state, leading to a major collapse of the high-ionization lines accompanying the drop in the X-radiation. The slow changes are attributed to gradual shifts in the wind interaction geometry between η Car A and B. The rapid variation is believed to be a temporary collapse of the wind interface (shock cone) due to the rapid periastron passage.

Direct detection of the hot η Car B has proven to be difficult as, at visible and IR wavelengths, the extended primary wind enshrouds the binary system. The wind of an early WN or an O-star has a mass-loss rate comparable to η Car B (Pittard & Corcoran 2002), but few massive stars have a terminal velocity of 3000 km s^{-1} . Verner et al. (2002) and Verner, Bruhweiler & Gull (2005) used photoionization CLOUDY models to replicate the combined spectrum of the Weigelt condensations B and D. They concluded that the excitation of the condensations during the spectroscopic low state was supported by the ultraviolet (UV) flux of η Car A, but during the spectroscopic high state the far-UV flux from a hotter η Car B, possibly a mid-O main-sequence star with $T_{\text{eff}} = 32\,000\text{--}37\,000 \text{ K}$, was necessary to excite the lines of [Ar III], [Ne III], [S III] and [Fe III]. With η Car A's characteristic $15\,000 \text{ K}$ temperature (Hillier et al. 2001, 2006), the scattered radiation of its wind dominates the spectrum from the UV to the IR. Most of the far-UV radiation seen by Far Ultraviolet Spectroscopic Explorer (FUSE) is scattered, and greatly modified, radiation from η Car B. Most of the far-UV radiation disappeared a few weeks before the mid-2003 drop in X-ray flux (Iping et al.

2005). Hence, the more energetic far-UV radiation necessary to create Ar^{2+} , Ne^{2+} , Fe^{2+} and S^{2+} disappeared in parallel with the X-radiation.

In the absence of direct signatures of η Car B, focus has been on spectral features formed in the wind–wind interface. Steiner & Damineli (2004) and Stahl et al. (2005) detected He II in the spectrum of η Car. Martin et al. (2006b) pointed out that the He II emission must originate near a wind–wind interface, not in the wind spectrum of a $15\,000 \text{ K}$ star. Nielsen et al. (2007b) pursued the idea of lines formed in the bow shock and analysed the He I wind profiles from the central 0.127-arcsec core using *Hubble Space Telescope*/Space Telescope Imaging Spectrograph (*HST*/STIS) CCD moderate dispersion spectra. They found that the He I absorption and emission also originated near the interface of the two winds – not from the secondary star atmosphere, but located well within the stellar core as seen by *HST*/STIS.

This paper takes another step to spatially characterize the wind interface. This is an analysis of *HST*/STIS observations obtained between 1998.0 and 2004.3, plus ground-based Very Large Telescope/Ultraviolet Visible Echelle Spectrograph (VLT/UVES) observations that overlap from late 2002 to 2004.3 and carry forward to early 2008. With *HST*/STIS long aperture spectroscopy, we have identified spatially extended, velocity-resolved forbidden emission lines that originate from low- and high-ionization species, associated with the extended wind and the wind interaction zone.

Forbidden lines of Fe^+ (in this paper defined as low ionization) originate from regions photo-excited by mid-UV radiation and with critical densities, $n_c \sim 2 \times 10^7 \text{ cm}^{-3}$. Such are the conditions in the outer portion of η Car A's wind and near the wind interaction zone. Forbidden lines of Ne^{2+} , Ar^{2+} , S^{2+} and Fe^{2+} (in this paper defined as high ionization) require far-UV radiation in regions with densities of 5×10^5 to $2 \times 10^7 \text{ cm}^{-3}$. These lines originate in the vicinity of the wind interaction region which spatially extends to considerable distance from the binary. By contrast, the permitted lines of H I and Fe II are emitted and absorbed throughout the stellar atmospheres and the extended wind. The permitted lines, with the bulk of emission within the 0.1-arcsec spatial resolution of *HST*/STIS, are centred on system velocity with a broad, asymmetric line profile that changes with orbital phase.

This paper qualitatively describes properties of the extended wind based upon *HST*/STIS and VLT/UVES spectroscopy. Section 2 describes the observations. Section 3 describes spectro-images of selected lines, showing the spatial and velocity extent with changing ionization and excitation, and apparent changes due to orbital phase and variation with position angle (PA). Spectro-images of lines formed in the vicinity of Weigelt D are included in the discussion. Section 4 presents a model to explain changes in emission structure, namely the extended wind is shaped as a distorted paraboloid by the wind interaction and is selectively ionized by mid- and far-UV radiation from the central source. Insights on the geometry of the system are derived from this working three-dimensional model that still requires a more detailed treatment. Section 5 is a discussion of the orbit based upon observations and model, followed by Section 6, which summarizes what we have observed and our interpretations.

Throughout the paper, we use the terms spectroscopic low and high state. The spectroscopic low state is the portion of η Car's 5.54-year period when the ionization/excitation of the system is supported only by mid-UV radiation from η Car A. This occurs across the periastron passage of η Car B and lasts for 3–6 months. The spectroscopic high state extends through most of η Car's period when the ionization/excitation is increased by the far-UV radiation from η Car B. We use compass directions (north-west = NW,

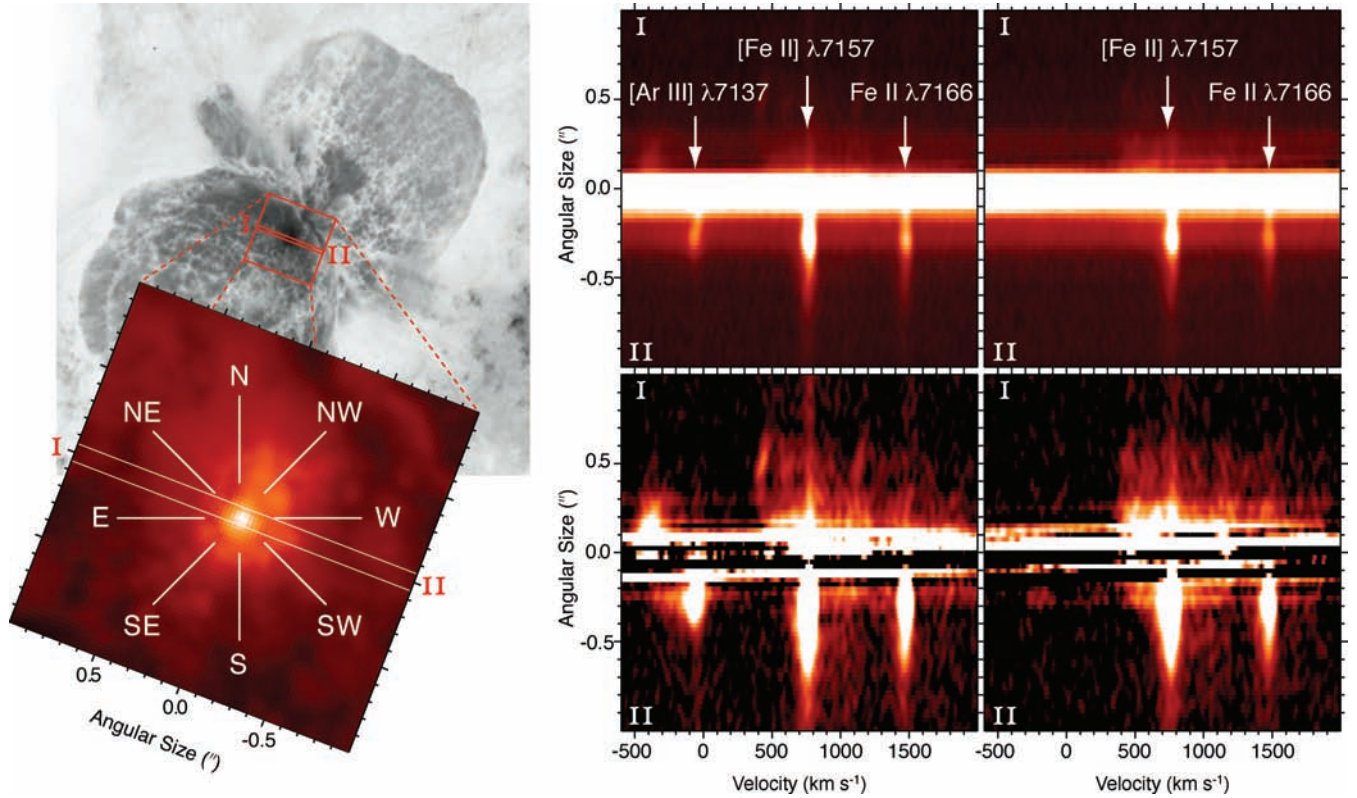


Figure 2. Example of *HST*/STIS spatially- resolved spectra in original form and modified with continuum subtraction. Top left: a *HST*/ACS HRC image of the Homunculus and η Car with 20-arcsec field of view. Bottom left: enlarged central 2-arcsec field of view with the 52×0.1 arcsec² aperture positioned at PA = +69°. Note the directional labels for reference in the paper including NW = northwest, etc. The spectro-images in the middle and right-hand columns were recorded from the central 2×0.1 arcsec² portion of the aperture as drawn between I and II in this figure. Centre and right: spatially resolved line profiles of [Ar III] λ 7137, [Fe II] λ 7157 and Fe II λ 7166 recorded at PA = +69°, 1 year apart [top centre: in 2002 July ($\phi = 0.820$) and top right: in 2003 July ($\phi = 1.001$)]. Bottom centre and right: the same STIS spectro-images displayed with continuum, referenced to 7210–7225 Å, subtracted on a spatial row-by-row basis. The [Ar III] is present in the 2002 July observation, but has disappeared in 2003 July. The [Fe II] and Fe II remain with relatively minor changes. The velocity scale is referenced to the vacuum rest wavelength of [Ar III] λ 7137 and the colour level display is proportional to $\sqrt{\text{Intensity}}$.

etc.) in our descriptions of the spatial extent of the wind emission (see Fig. 2). All wavelengths are in vacuum and velocities are heliocentric.

2 OBSERVATIONS

The Homunculus, a very bright reflection nebula, contaminates observations of η Car especially from the ground. Imaging spectroscopy with *HST*/STIS uniquely provides the spatial resolution necessary to separate the spectra of η Car and its extended wind from the nebula. We used extracted portions of observations recorded with the STIS CCD (0.0507 arcsec pixel^{−1} scale) with medium dispersion gratings ($R \sim 8,000$) in combination with the 52×0.1 arcsec² aperture from 1640 to 10 100 Å to sample the spectrum of the central core at pre-selected phases. *HST* solar panel Sun-orientation requirements constrain the range of STIS aperture PAs that shifts continuously throughout the calendar year. Hence, it was not possible to do time-critical observations with the same PA. Fortunately, the observations at arbitrary PAs led to greatly increased insight on the extended wind and ultimately to this discussion.

The first complete STIS CCD spectrum of η Car was recorded during the spectroscopic low state of 1998 ($\phi = 0.007$) at PA = −28° (see Table 1). A second complete STIS CCD spectrum of η Car was recorded a year later (1999.2, $\phi = 0.213$) at the same PA. Additional proposals to Guest Observer (GO) and Guaranteed Time Observations (GTO) programmes continued observations across the

broad spectroscopic high state. A series of observations, designed to follow changes across the 2003.5 low state, began in summer of 2002 and extended through 2004 March. The Weigelt condensation, D, located 0.25 arcsec NNW from η Car (Fig. 1) was monitored along with the central star. Where necessary, additional critical observations of Weigelt D were added when the PA range prevented inclusion in the long aperture centred on η Car. Separate, complete spectra of Weigelt D were obtained in 2002 July (late high state, $\phi = 0.820$) and 2003 July (early low state, $\phi = 1.001$) at PA = +69°.

We used the reduced STIS CCD spectra available through the STIS archives (<http://archive.stsci.edu/prepds/etacar/>). The STIS optical design (Kimble et al. 1998; Woodgate et al. 1998) incorporates spectroscopic and imaging modes selected via a three-axis mechanism that rotates a specific grating into the optical beam and tilts the grating to place the desired spectral range on to the detector format. The result is that the spectrum of a point source is slightly tilted with respect to the CCD rows and columns. The tilt changes by small amounts with each return to a specific wavelength setting, incrementally affecting the spectral format. This causes problems when attempting to extract a stellar spectrum at spatial resolutions approaching *HST*'s diffraction limit. A specific data reduction tool to alleviate this problem for the η Car CCD spectra was developed by K. Ishibashi and K. Davidson (<http://archive.stsci.edu/prepds/etacar/>). The extracted spectra of the η Car central core and the Weigelt condensations have been

Table 1. *HST*/STIS data used in this analysis. All spectra are recorded with the G430M or G750M grating.

<i>HST</i> programme	Observation date	JD (−245 0000)	ϕ^a	PA (°)
7302 ^b	1998 March 19	0891	0.045	−28
8036 ^c	1999 February 21	1231	0.213	−28
8483 ^c	2000 March 20	1623	0.407	−28
8619 ^b	2001 April 17	2017	0.601	22
9083 ^b	2002 January 19–20	2294	0.738	−82
9337 ^b	2002 July 4 ^d	2460	0.820	69
9420 ^b	2003 February 12–13	2683	0.930	−57
	2003 March 29	2727	0.952	−28
	2003 May 5 ^d	2764	0.970	27
	2003 May 17 ^d	2776	0.976	38
	2003 June 1	2792	0.984	62
	2003 June 22 ^d	2813	0.995	70
9973 ^b	2003 July 5 ^d	2825	1.001	69
	2003 July 29 ^d	2851	1.013	105
	2003 September 22	2904	1.040	153
	2003 November 17	2961	1.068	−142
	2004 March 6	3071	1.122	−28

^aPhase, ϕ , relative to the *RXTE* minimum at 1997.9604 (Corcoran 2005): JD 245 0799.792+2024 $\times \phi$.

^b*HST* GO Programme – K. Davidson, Principal Investigator (PI), see http://www.stsci.edu/hst/scheduling/program_information.

^cSTIS GTO Programme – T. R. Gull (PI).

^dIncluding observation of the Weigelt D.

Table 2. Data used in this analysis made with VLT/UVES.

VLT programme ^a	Observation date	JD (−245 0000)	ϕ^b
070.D-0607	2002 December 07	2616	0.897
	2002 December 12	2621	0.901
	2003 February 14	2685	0.931
071.D-0168	2003 May 29	2789	0.983
	2003 June 1	2792	0.985
	2003 July 5	2825	1.001
074.D-0141	2005 February 12	3414	1.291
	2005 March 19	3449	1.309
077.D-0618	2006 April 9	3835	1.499
	2006 June 8	3895	1.529
380.D-0036	2008 January 11	4477	1.817

^aAll observations under VLT/UVES programmes – K. Weis (PI).

^bPhase, ϕ , relative to the *RXTE* minimum at 1997.9604 (Corcoran 2005): JD 245 0799.792+2024 $\times \phi$.

discussed elsewhere (Zethson 2001; Davidson et al. 2005; Martin et al. 2006b; Nielsen, Ivarsson & Gull 2007a).

Seeing-limited, ground-based observations provide temporal variations of the overall wind structure as first noted by Zanella, Wolf & Stahl (1984). A campaign to complement the *HST*/STIS observations with ground-based VLT/UVES observations (Table 2), extending from 3040 to 10 430 Å, was headed by K. Weis. Spectra were obtained frequently across the 2003.5 low state and at intervals across the high state through 2008.0. The VLT/UVES spectra were recorded through a long slit (8 and 12 arcsec lengths with 0.4 and 0.3 arcsec width for the red and blue arms of the spectrograph), extending well beyond the stellar component of η Car. All VLT/UVES high-dispersion spectra ($R \sim 80\,000$ and $110\,000$ in the blue and red) were obtained with the same position angle, PA = +160°. While there is overlap with *HST*/STIS from late 2002 to early 2004,

the loss of STIS led to no high-spatial-resolution coverage beyond 2004 March. Hence, we discuss *HST*/STIS and VLT/UVES spectra, recorded at similar phases, but not necessarily the same temporal period. We are unable to address variations between periods and long-term trends with the available data.

A spatially resolved, line-by-line data reduction was performed by O. Stahl on the recorded VLT/UVES spectra. For each observation, the stellar profile was measured along the length of the slit and extractions were performed down to the 10 per cent intensity level of the peak (Nielsen, Gull & Vieira Kober 2008). The spatial extraction widths ranged from 2 to 3 arcsec, significantly larger than the observer-logged seeing conditions.

3 THE SPATIALLY-RESOLVED LINE PROFILES

The *HST*/STIS CCD spectra show that most broad lines have faint spatially resolved emission components. Many of these features, previously noted as unidentified lines in the spectrum of the Weigelt condensations (Zethson 2001), prove to be narrow, spatially resolved components of both high- and low-ionization forbidden wind lines from extended wind structures.

Fig. 2 shows examples of resolved, broad forbidden lines of both low and high ionization. Faint spatially and velocity-resolved emission lines were observed in [Ar III] $\lambda 7137$, [Fe II] $\lambda 7157$ and Fe II $\lambda 7166$ against the bright nebular emission and dust-scattered stellar radiation. The spatially resolved lines include strong, narrow-line emission from the SW of η Car not previously noted by Weigelt & Ebersberger (1986). Weak, but observable, spatially resolved velocity arcs extend from both sides of the stellar position. We used the merged spectrum of Weigelt B and D, as published by Zethson (2001), which includes strong scattered starlight to select clean segments of the continuum close to the wavelength of the wind line of interest. We then subtracted the averaged continuum on a spatial row-by-row basis (in the STScI available data set, each resampled row is spaced 0.025 arcsec = 1/2 pixel along the STIS aperture) to increase the visibility of the line emission. Row-by-row continuum subtraction across the star position was less successful due to insufficient correction in the data reduction for small tilts of the spectrum on the CCD format in the spectro-image. Independent five row, 0.128-arcsec wide, extractions centred on the stellar position confirm that the broadened, forbidden line emission extends across the stellar spectrum (see the STIS line profiles in Fig. 3).

In 2002 July ($\phi = 0.820$), the [Ar III] $\lambda 7137$ emission (Fig. 2, Centre) extends as two diffuse arcs, one from 0 to −300 km s^{−1} extending 0.3 arcsec WSW of η Car and a second from −500 to −300 km s^{−1} extending 0.3 arcsec in the ENE direction from η Car. The [Fe II] $\lambda 7157$ emission is traceable to greater distances at ± 400 km s^{−1} with faint, wispy arcs to the ENE out to 0.6 arcsec at −400 km s^{−1}. The [Fe II] is blended on the red side with Fe II $\lambda 7166$ emission, separable because of similar spatial and velocity distributions. In 2003 July ($\phi = 1.013$), the [Ar III] emission is absent as demonstrated by ground-based spectrophotometry (Damineli et al. 2008). The [Fe II] and Fe II emissions remain with spatial structure similar to that seen in 2002, but with slight variations in intensity.

The VLT/UVES spectra, with high spectral resolution but seeing-limited spatial resolution, provide measures of the averaged emission from the stellar source, the extended wind and the bright narrow-line emission from the Weigelt condensations, all included in the 1–3 arcsec seeing disc. As noted by Damineli et al. (2008), the [Ar III] narrow-line component drops as periastron approaches and recovers 6–8 months later. The UVES spectral profiles, plotted in

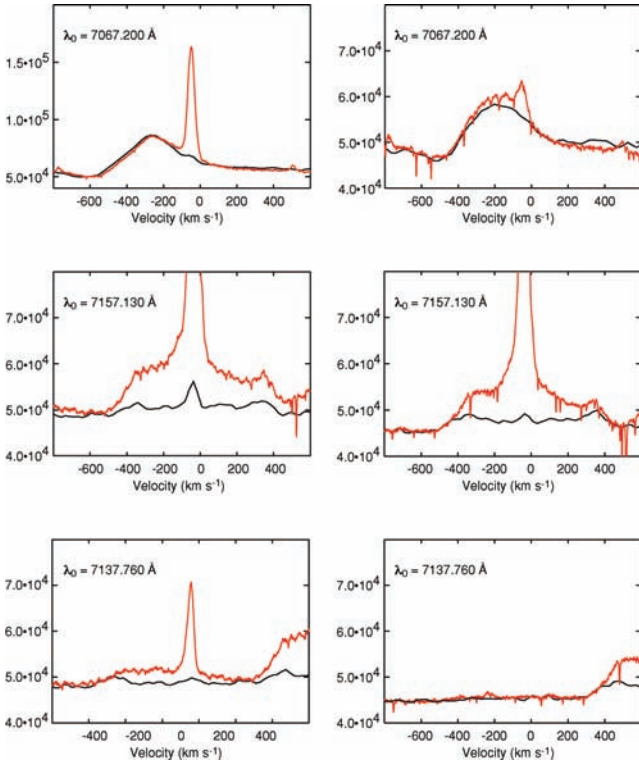


Figure 3. Examples of spectra, centred on η Car, recorded with VLT/UVES and *HST*/STIS in 2003, differing by angular resolution and aperture size. The VLT/UVES (black line) is seeing-limited at 1 to 2 arcsec while *HST*/STIS (red line) is near diffraction limited at 0.1 arcsec. All spectra are normalized to the local continuum. Left-hand column: observations on 2003 June 1 ($\phi = 0.985$). Right-hand column: observations on 2003 July 5 ($\phi = 1.001$). Top row: He I $\lambda 7067$ profiles as measured by the instruments, excluding the narrow-line component contribution from the Weigelt condensations, are very similar during both the spectroscopic low and high states. Centre row: [Fe II] $\lambda 7157$ profile, sampled by VLT/UVES, has a broad component marginally detected by *HST*/STIS. Bottom row: the [Ar III] $\lambda 7137$, seen in the VLT/UVES spectrum at $\phi = 0.985$, has a broad component that is not seen by *HST*/STIS. In general, He I and H I line profiles track well, while all forbidden lines, both low and high ionization, do not. Investigation with the *HST*/STIS spectra led to the realization that broad components of forbidden emission lines originate from extended regions, unlike the He I and H I emission, which originates deep within the central core (Nielsen et al. 2007b; Weigelt et al. 2007).

Fig. 4, show a similar decline going into periastron and slow recovery through 2006. The broad component of [Ar III] $\lambda 7137$ reaches its maximum intensity in 2006 ($\phi = 1.499$) and then slowly declines. By contrast, the [Fe II] broad component is bright in 2005 April ($\phi = 1.291$), then weakens. The [Fe II] emission is phase shifted compared to the [Ar III] emission. The line profiles recorded with VLT/UVES of [Ne III], [S III] and [Fe III] behave similarly to those of [Ar III]. A pattern of phase shift emerges between low- and high-ionization species, which is confirmed in earlier cycles of η Car's 5.54-year spectroscopic period (Damineli & Teodoro, private communication).

3.1 Variations with ionization potential and excitation

Both forbidden and permitted broad lines are present throughout the 1640–10 430 Å spectral region sampled. Longwards of 4000 Å the broad lines become increasingly isolated and easier to analyse.

The forbidden lines, as they have no absorption component and as most of the electron and dust scatterings are associated with higher density, interior wind and atmospheres, provide a clearer sample throughout the extended structure. Hence, the forbidden line profiles reveal spatially and velocity-resolved slices of the extended wind structure. The broad permitted lines of H I and Fe II originate from the dense, optically thick stellar wind, with the Fe II lines originating at larger radii than the H I lines (Hillier et al. 2001, 2006). When both H I and Fe II lines are present, classic stellar wind models predict associated P Cygni absorption. However, with the exception of the high members of the H I Balmer series, this absorption is seen only during the low state for H I and Fe II lines. (Nielsen et al. 2007b).

By contrast, each forbidden line originates in regions with densities near the line's collisional critical density. As stellar winds are usually denser than the critical density, the wind component of these lines is generally weak in normal stellar wind spectra. Their strength is further controlled by the ionization structure – a specific ion exists only in the regions of the wind or atmosphere where photoionization can produce that ion. High-ionization species (e.g. Fe²⁺, Ne²⁺, Ar²⁺, S²⁺) are produced by far-UV photons while mid-UV photons are responsible for the low-ionization species (e.g. Fe⁺). Less energetic photons, or more likely collisions, are sufficient to populate the meta-stable state leading to forbidden line emission.

The different broad lines (Table 3) can be sorted into four categories dependent upon ionization and spatial structures as seen by *HST*/STIS spectro-images:

- (i) broad permitted lines originating from within 0.1-arcsec central core,
- (ii) high-ionization, blue-shifted forbidden lines that are observed in *HST*/STIS spectro-images as arcs and, at some PAs, spatial/velocity rings,
- (iii) low-ionization permitted lines with spatially and velocity-resolved filled structures,
- (iv) low-ionization forbidden lines that have multiple rope-like structures, centred on the system velocity.

The near diffraction-limited spatial resolution plus moderate spectral dispersion of the *HST*/STIS CCD mode is well matched to resolve broad lines of η Car as presented in Figs 5 through 10. For these, and subsequent figures showing spectro-images, an *HST*/Advanced Camera Surveys (ACS) High Resolution Camera (HRC) 2×2 arcsec² image (Fig. 5, left-hand panel) is included as a reference for the orientation and position of the central 2-arcsec portion of the STIS 52×0.1 arcsec² aperture through which the spectra were recorded. As only a few *HST*/ACS HRC images were recorded during these studies, we chose to show the same image, recorded in 2003 February ($\phi = 0.930$) with the 550M filter, for each set of spectro-images.

All spectro-images in Figs 5 through 10 were extracted from *HST*/STIS CCD spectra recorded at PA = +38° on 2003 May 5 ($\phi = 0.970$). The colour scale for each spectro-image is proportional to $\sqrt{\text{Intensity}}$. The velocity scale is ± 600 km s⁻¹. Note that the high spatial resolution of *HST*/STIS is recording only a thin slice of a much more extended region. Multiple spectro-images of this nature across the central 2-arcsec region, when co-added, produce the wind profile as seen with VLT/UVES.

3.1.1 Line formation within 0.1 arcsec

Hydrogen line profiles are difficult to interpret as the emission originates throughout the optically thick stellar atmospheres and

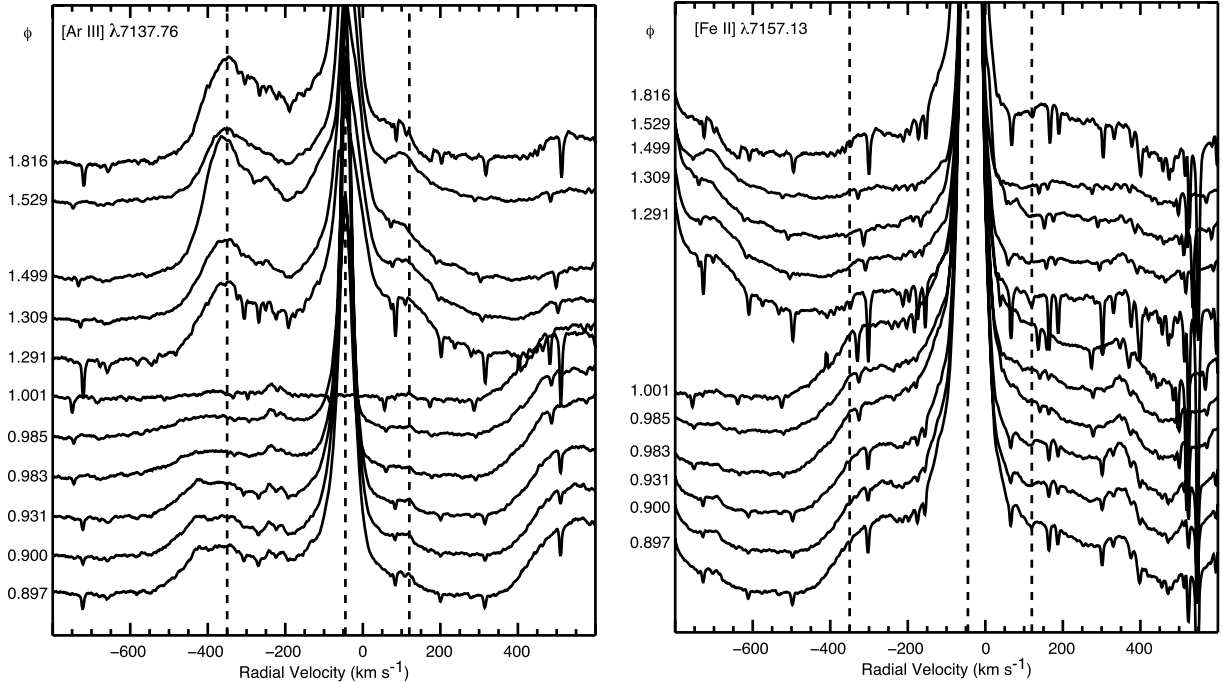


Figure 4. UVES-obtained line profiles of [Ar III] $\lambda 7137$ (left-hand panel) and [Fe II] $\lambda 7157$ (right-hand panel). The blue-shifted component of the [Fe II] broad-line profile is strongest near the minimum ($\phi = 1.001$) and weakens as the system reaches apastron ($\phi = 1.499$). By contrast, the [Ar III] line disappears during the spectroscopic minimum, then rebuilds through apastron. The variable narrow absorption lines are terrestrial in origin.

wind. The high optical depths lead to absorption, especially by intervening, cooler, outer parts of the winds. The blue-shifted portion of the emission is greatly modified by extended winds leading to a characteristic P-Cygni profile. Weigelt et al. (2007) measured the 50 per cent encircled energy diameters of H I Br γ at 2 μ m to be 9.6 mas, well within the 0.1-arcsec angular resolution of *HST*/STIS CCD spectral modes. None the less, the continuum-subtracted spectro-image reveals a faint, spatially extended shell in H I $\lambda 6564$ (Fig. 5, right-hand panel). By contrast, the low-ionization (7.9 eV), permitted Fe II $\lambda 4815$ broad line (Fig. 10, right-hand panel) has a solid core of emission, but a more robust diffuse, extended structure associable with wind.

Helium emission and absorption are largely constrained to the central 0.1-arcsec core, as previously discussed in detail for He II (Martin et al. 2006b) and for He I (Nielsen et al. 2007b). An excitation potential (EP) of 51 eV is required to populate the upper level of the He II $\lambda 4686$ transition after an interaction removing the first electron with an ionization potential (IP) of 24.6 eV (see Table 3). The faint He II $\lambda 4686$ originates from the wind interaction in the vicinity of the stagnation point of the shock cone, where the X-rays form (Pittard & Corcoran 2002). The He II $\lambda 4686$ emission is weak until about 6 months before the X-ray drop. As with all high-excitation lines, it drops precipitously as the X-ray flux quickly disappears and slowly reappears. While He II $\lambda 4686$ emission originates from the wind–wind boundary, the energetics are uncertain. Martin et al. (2006b) suggest that the origin is related to the close approach of the two stars during the spectroscopic low state and possibly indicate mass transfer or ejection in addition to mechanisms associable with the shock surface of η Car B’s wind. Weak He II $\lambda 4686$ emission is seen in scattered radiation off Weigelt D several months before the periastron passage. The *HST*/STIS spectra show no evidence of He II $\lambda 4686$ during the low state or most of the high state.

The He I wind lines are confined primarily to the central 0.1-arcsec core. Weigelt et al. (2007) measured the 50 per cent encir-

led energy to be within 6.5 mas, well within the H I Br γ size. The He I lines studied by Nielsen et al. (2007b) require >20 eV to excite their upper levels. However, above a certain density, n_c , collisions rapidly deplete the metastable energy states leading to decreased emission. Densities in the wind interaction structure change throughout the period as demonstrated by the behaviour of permitted He I wind lines. Nielsen et al. (2007b) noted that, as periastron approached, the ratio of the He I triplet relative to singlet-wind absorption increased. The dominant excitation of He I changed from photo-excitation at distant apastron to contributions from collisions as η Car A and η Car B neared periastron due to effects from higher density and optical depth. As shown in Fig. 6 (left-hand panel) for He I $\lambda 6680$, some spatial extension similar to that seen in H I $\lambda 6564$ is present in all He I lines. Especially notable in the He I spatial structure is the absorption component that extends above and below the stellar position but shifts to the red on either side. The absorption width is broader to the SW than to the NE. Similar effects are traceable on deeper displays of the H I spectro-images. These absorptions originate in the outer winds but become increasingly confused with distance from η Car due to scattered light from the dusty Homunculus.

3.1.2 High-ionization forbidden lines

In a stellar wind of uniform temperature and ionization, and for a simple two-level atom, the bulk of the emission due to collisions arises in regions with densities close to the critical density (e.g. Hillier 1988), where the critical electron density is the electron density at which half of the decays from the upper level are by radiative processes, while the rest are collisionally de-excited.

The far-UV radiation from η Car B leads to highly ionized regions extending outwards from the low-density wind of η Car B. In the vicinity of the extended wind interaction, gas compresses leading to collisional excitation and increasing emission of the

Table 3. Species that characterize the spatial/velocity structure.

Structure	Spectrum	IP ^a (eV)	EP ^b (eV)	λ_{vac} (Å)	n^c_c (cm ⁻³)
Inner region	He II	24.6	51.0	4686	
	He I	0	23.1	6680	
			23.1	5878	
			22.7	7067	
			12.1	6564	
Intermediate 'high' ionization	He I	0	23.1	6680	
			23.1	5878	
			22.7	7067	
	H I	0	12.1	6564	
	[Ne III]	41.0	3.2	3868 ^d	1×10^7
			3.2	3968 ^e	
	[Ar III]	27.6	1.7	7137	4×10^6
			1.7	7753 ^f	
			4.1	5193 ^f	
Blue-shifted structures	[S III]	23.3	3.4	6313	2×10^7
			1.4	9071	5×10^5
			1.4	9533	5×10^5
	[Fe III]	16.2	2.7	4659	$\sim 10^7$
			2.7	4702	
	[N II]	14.5	4.1	5756	3×10^7
Extended wind	H I	0	12.1	6564	
	Fe II	7.9	5.5	5318	
Low-ionization boundaries	[Fe II]	7.9	2.0	7157	2×10^6
			2.8	4815	2×10^6

^aIonization potential required to reach this ionization stage.^bExcitation potential to excite the transitional upper level.^cCritical electron densities from Osterbrock & Ferland (2006), Appenzeller & Oestreicher (1988) and CMFGEN models by Hillier et al. (2001, 2006).^dSome blending.^eHighly blended.^fWeak.

high-ionization forbidden lines until the critical density is reached. The high-ionization forbidden emission lines thus originate from a relatively thin region directly photoionized by η Car B within the wind interaction zone. Dependent upon ionization potential, temperature and critical density (see Table 3), the spectro-images of lines of different ions, and internal upper levels, will reveal different but related thin regions.

Ionization to Ne²⁺ requires 41.0 eV but far less photon or collisional energy (3.2 eV) to excite the upper level of [Ne III] λ 3869. The upper level is damped at a critical density of 5×10^5 cm⁻³. At PA = +38° and $\phi = 0.970$, the spectral-image (Fig. 6, right-hand panel) shows an arc extending from -550 km s⁻¹, 0.2 arcsec NE to -250 km s⁻¹, 0.25 arcsec SW, plus a segment of narrow emission at -40 km s⁻¹ extending 0.25 arcsec NE to 0.25 arcsec SW. It is strongest on the SW portion. A second [Ne III] line at 3968 Å has similar structure but is heavily blended. Likewise, other lines of [Ar III], [S III], [Fe III], [N II] and [Fe II] have spatially extended broad-line structures but are blended with other spectral features, often confused by absorption from permitted Fe II or H I wind lines originating from the core. We present the best, representative examples in the discussion below and note where blending or contamination is significant.

The ions, Ar²⁺ and S²⁺, have similar ionization potentials (27.6 and 23.3 eV) and thus the [Ar III] λ 7137 and [S III] λ 9533 wind lines (Fig. 7, left- and right-hand panels) have similar spatial structures.

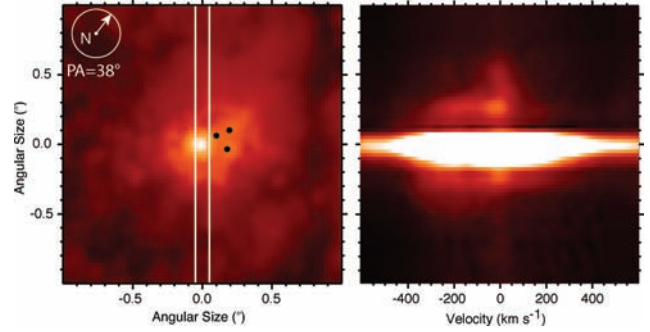


Figure 5. Spatial/velocity emission of selected lines. Left-hand panel: *HST*/ACS HRC image of central 2 arcsec centred on η Car with overlay of 2-arcsec long portion of the *HST*/STIS 52×0.1 arcsec² aperture at PA = 38°. This series of spectro-images were recorded on 2003 May ($\phi = 0.976$). Right-hand panel: H I λ 6564 spectro-image with continuum subtraction. The extended emission is very weak compared to the stellar emission. Hence, this spectro-image is displayed logarithmically to reach the faint extended structure. The remaining spectro-images are displayed with colour scale proportional to $\sqrt{\text{Intensity}}$.

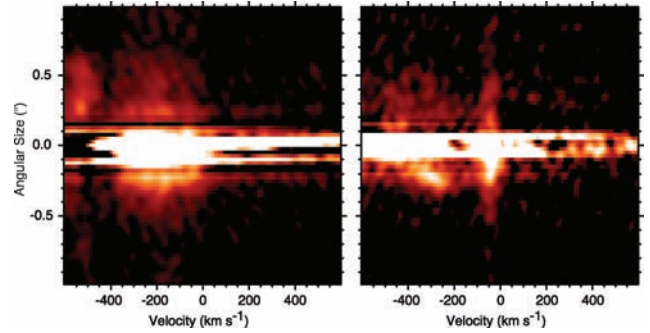


Figure 6. Left-hand panel: He I λ 6680 emission originates primarily from the apex of the wind interaction regions well within the 0.1-arcsec stellar core as demonstrated by Nielsen et al. (2007b). However, some weak emission extends beyond the 0.1-arcsec inner region. Right-hand panel: [Ne III] λ 3869 appears as a partial arc extending from -40 to -550 km s⁻¹ near the core position. Neon is doubly ionized by far-UV radiation from the central source and the emission originates from regions where electron densities are near the critical density.

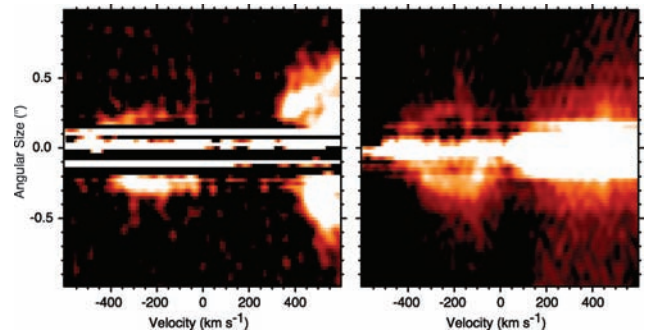


Figure 7. Left-hand panel: [Ar III] λ 7137 forms a nearly complete arc extending on both sides on the central core. The bright emission longwards of 400 km s⁻¹ is from nearby [Fe II] λ 7157. Right-hand panel: [S III] λ 9533 has a very similar structure. The bright stellar emission longwards of 0 km s⁻¹ in the [S III] λ 9533 spectro-image is from H I λ 9549.

The arc seen in [Ne III] is now a nearly complete ring extending from 0 to -550 km s^{-1} and spatially out to 0.2 arcsec NE and 0.3 arcsec SW. The [S III] spectro-image is contaminated to the red by H I $\lambda 9549$ which might absorb significant red-shifted radiation. However, the bulk of the hydrogen emission and absorption appear to be from the central core. Its extended emission is weak. Little absorption is apparent in the Paschen lines. Comparisons to other high-excitation spectro-images indicate that absorption does not substantially affect the visibility of the [S III] emission.

Both [Fe III] $\lambda 4659, 4701$ spectro-images are presented in Fig. 8 as each is contaminated on the red side by other lines. The [Fe III] $\lambda 4659$ line is affected by [Fe II] $\lambda 4665$, plus several weaker narrow emission lines from Weigelt B and D. The faint emission to the red originates entirely from the [Fe II] $\lambda 4665$ wind line that extends out to 0.6 arcsec NE and 0.5 arcsec SW as seen in [Fe II] $\lambda 7157$ in Fig. 9 (right-hand panel). Longwards of [Fe III] $\lambda 4702$ is the He I $\lambda 4714$ wind line with a strong absorption component. The He I emission and absorption originates from the inner 0.1-arcsec core. Hence, absorption by He I $\lambda 4714$ of the [Fe III] $\lambda 4702$ emission is negligible, but can lead to a baseline offset in the total flux. While no other highly excited forbidden line shows a red component at this position, we are unable to show a completely isolated line of [Fe III]. Therefore, we track two separate lines of [Fe III] in the following discussion. Several weaker [Fe III] lines nearby in the spectrum, while blended, show no evidence of a red component. Even though

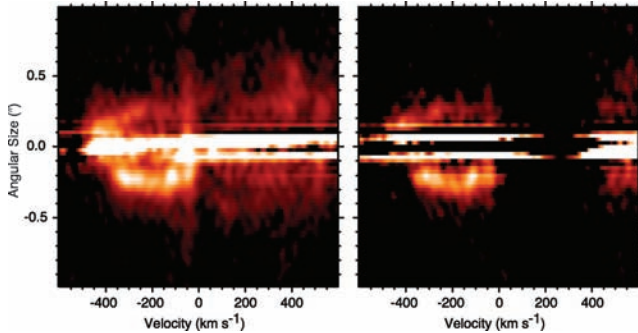


Figure 8. Left-hand panel: [Fe III] $\lambda 4659$ appears in a complete arc. Weak emission, to the red in the [Fe III] $\lambda 4659$ spectro-image, is due to a nearby [Fe II] line. Right-hand panel: [Fe III] $\lambda 4702$ shows up in the same arc. Strong absorption redward of [Fe II] $\lambda 4701$ is from He I $\lambda 4714$ that originates in the central core and is seen as scattered light in the extended wind structure.

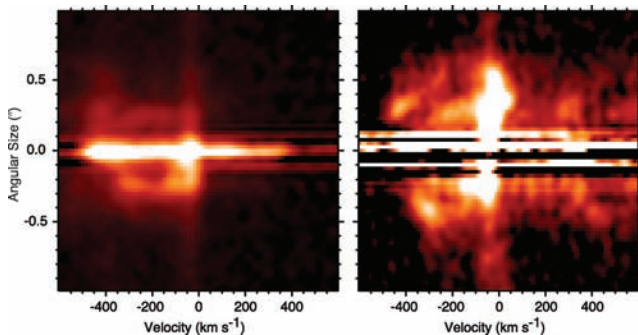


Figure 9. Left-hand panel: [N II] $\lambda 5756$. Right-hand panel: [Fe II] $\lambda 7157$. The difference in ionization potential between the two species leading to these forbidden lines is reflected in the structures of the outer bow-shock emission and the outer regions of η Car A's wind.

the ionization potential of Fe^{2+} is 16.2 eV, substantially lower than IP's for Ar^{2+} and S^{2+} , the [Fe III] lines extend to velocities and distances similar to those of the [Ar III] and [S III] lines.

The [N II] $\lambda 5756$ wind line is strong and located in a spectral region with few other lines. As seen in Fig. 9 (left-hand panel), the line structure is quite similar to what is seen in the [Fe III] lines (Fig. 8). The emission begins at -40 km s^{-1} , extends blueward to -550 km s^{-1} , and spatially from 0.25 arcsec NE to 0.3 arcsec SW. The narrow-line component centred at -500 km s^{-1} is from [Fe II] $\lambda 5748$. This ring structure persists for all high-ionization forbidden lines. However, the broad component, seen in [N II] centred on the 0.1-arcsec central core and extending from -550 to $+400 \text{ km s}^{-1}$, is not strong in the higher ionization forbidden lines. The forbidden emission from N^+ , with IP of 14.5 eV, not that dissimilar from the IP leading to H^+ comes from an upper energy level with a significantly higher critical density than the emission of [Fe III]. The [N II] emission originates not only from lower ionized portions of the wind interaction zone but also in the low-ionization, higher density regions within the central core. [N II] represents the transition from the high-ionization to the low-ionization regions.

In essence, the high-ionization forbidden lines, originating from ions of descending IP, describe increasingly more distant slices of the η Car B photoionized wind interaction regions as the more energetic UV photons are depleted.

3.1.3 Low-ionization forbidden/permitted lines

Iron ionizes to Fe^+ by 7.9 eV radiation or collisions (and potentially charge exchange), but only a small increment to 16.2 eV is required to reach Fe^{2+} . These IPs bracket that of N^+ at 14.5 eV. Collisions and photo-excitation to upper Fe^+ energy levels can be sufficient to populate many metastable levels, some at relatively low-energy levels above the ground state. Moreover, many Fe II permitted transitions lead to strong wind lines from the near-UV to near red spectral regions. We show two examples of [Fe II] wind lines, at 7157 Å close to the [Ar III] $\lambda 7137$ wind line (Fig. 9, right-hand panel) and at 4815 Å (Fig. 10, left-hand panel). The [Fe II] emission forms double arcs with the outer arc extending outwards to ± 0.75 arcsec and from -500 to $+400 \text{ km s}^{-1}$. The inner arc is similar to the structure seen in the [Ar III] and [Fe III] lines, but displaced spatially outwards. The outer arcs, best defined on the blue side, define an outer boundary, or rim, of the extended wind from η Car A. The [Fe II] emissions originate from lower excitation, lower density, outer regions of the

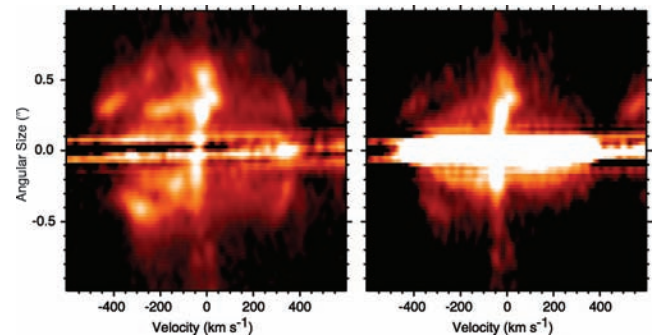


Figure 10. Left-hand panel: [Fe II] $\lambda 4815$. Right-hand panel: Fe II $\lambda 5318$. Note the very strong permitted emission on the stellar position for Fe II $\lambda 5318$. The weak Fe II diffuse, extended wind emission tapers off within the stronger [Fe II] rope-like emission.

extended wind and indicate those outer regions that are excited by collisions and/or mid-UV radiation from the binary filtered by the primary wind. The inner arc defines the denser, less ionized regions of the extended wind interaction zone facing η Car A.

The spectro-image of Fe II $\lambda 5318$ (Fig. 10, right-hand panel) reveals a decidedly more diffuse centrally biased emission than seen in [Fe II] $\lambda 4815$ (Fig. 10, left-hand panel). All other low-ionization, permitted lines have similar structures, defined by the central core and extended wind emission.

3.2 High ionization versus low ionization – a means to follow changes in the interacting wind structures

We have shown that the [Ne III], [Ar III], [S III] and [Fe III] lines have similar velocity and spatial structures for a single observation at a specific PA. The emission velocity and spatial structure seen in these lines track very well within each observation, but change notably with PA and phase. For clarity, we now limit the discussion to variations of the spectro-images of [Fe III] (16.2 eV) and [Fe II] (7.9 eV) across the 6-year interval. We follow the changes with three lines, [Fe III] λ 4659, 4702 and [Fe II] λ 4815. We track variations throughout the orbital period, gaining increased insight on the changes in ionization and structure with phase and PA.

Figs 11–14 display: (1) the *HST*/ACS HRC 2×2 arcsec² field of view; (2) the [Fe III] λ 4659; (3) the [Fe III] λ 4702 and (4) the [Fe II] λ 4815 spectro-images. Each ACS image is rotated to show the position of the long aperture, from which the 2-arcsec spectro-image extending ± 600 km s^{−1} has been extracted. Each ACS image includes a compass with needle pointing towards north along with the actual PA. Three dots indicate the location of Weigelt condensations B, C and D (see also Fig. 1). All spectro-images have been processed identically with a spatial row-by-row continuum subtraction, using a portion of the spectrum with no bright narrow- or broad-line contamination. Each is displayed with the same red colour scale proportionate to $\sqrt{\text{Intensity}}$.

The three lines displayed in Figs 11 through 14 have potential contamination due to narrow-line emission from the Weigelt condensations and stellar emission. The [Fe III] λ 4659 wind emission (Column 2) can be contaminated by up to five narrow lines: N I λ 4662; Fe II λ 4665; [Fe II] λ 4666; Fe II λ 4668 and [Fe III] λ 4659. The [Fe III] λ 4702 (Column 3) is contaminated by He I λ 4714 line profiles, demonstrated above to originate primarily in the stellar core. The He I line provides a background absorption profile in the scattered starlight, but does not absorb the forbidden radiation, physically emitted at distances well outside the binary orbit. The [Fe II] λ 4815 (Column 4) depicts low-ionization structure of the extended winds with little contamination.

A description of the spectral variations of η Car is that the high-ionization lines are strongly present for most of the 5.54-year orbit, but that they disappear for about 6 months beginning about the same time as the drop in X-rays. Both broad and narrow components drop quickly and undergo slow recovery with the highest ionization lines disappearing first and recovering last (Damineli 1996; Damineli et al. 2008). All VLT/UVES and *HST*/STIS spectra are consistent with this concept. Studies of the STIS far-UV and mid-UV echelle spectra of η Car (Nielsen, Gull & Vieira Kober 2005) suggested a decline in highly excited atomic states beginning about 6 months before the X-ray drop/spectroscopic minimum in 2003.5. Nielsen et al. (2009) demonstrated that the major drop of the high-ionization wind lines occurred with complementary growth of low-ionization wind lines.

3.2.1 Variations of ionization with phase

Observations of η Car with VLT/UVES continued following the 2003.5 low state to early 2008 ($\phi = 1.0$ –1.813). Relative to stellar continuum, the [Fe II] λ 7157 broad component was strongest in 2005 February ($\phi = 1.291$), eight months after the 2003.5 minimum, but then decreased. In contrast, the brightness of the [Ar III] λ 7137 broad component increased through 2006 April ($\phi = 1.499$), at the apastron portion of the period. Teodoro (private communication) examined the variation of [Ar III] λ 7137, as observed from 1993.5 to 1998.0, and confirmed that the broad component was strongest near $\phi = 0.5$. The limited evidence suggests that the behaviour of the broad components of high-ionization, forbidden lines is similar for at least the past three periods and that we can use these lines to gain insight on the periodic variations of the outer wind structure and the excitation by the central source.

Six sets of spectra, recorded at selected phases at PA = -28° , or PA = $+152^\circ = -28^\circ + 180^\circ$, led to the spectro-images shown in Fig. 11. For the benefit of the reader, the spectro-images in Fig. 11 (row 5), recorded at PA = $+152^\circ$, were mirror imaged in the spatial direction to display in the same aperture orientation.

Observations recorded during the two minima, $\phi = 0.045$ and 1.040 (rows 1 and 5), demonstrate the absence of both [Fe III] lines and the strengthening of the [Fe II] line in general, but especially to the NNW, which projects in the direction of Weigelt condensations B and D. By $\phi = 0.213$ (1.3 years past the X-ray drop), spatially and velocity-resolved components reappear very strongly from -40 to $+200$ km s^{−1} in both [Fe III] lines, extending NNW outwards to 0.3 arcsec, about the same projected distance as Weigelt condensation D. A much weaker component appears at -200 to -400 km s^{−1}, extending 0.2 arcsec to the SSE of η Car. The [Fe II] structure nearly disappeared to the NNW at $\phi = 0.213$, but is seen weakly at $\phi = 1.122$, a little more than one period later. The spectro-images taken at $\phi = 0.407$ (2.3 years past the X-ray drop) are similar to those at $\phi = 0.213$ except that all emission appears to be more developed at larger distances and velocities. One additional observation at PA = -28° was accomplished at $\phi = 0.952$ and shows notable differences in both low- and high-ionization lines. The [Fe III] lines disappeared at velocities above $+100$ km s^{−1}. The [Fe II] emission shows much stronger condensations centred on the stellar position and to the blue in the SSE. At $\phi = 1.040$, the [Fe III] disappeared, the [Fe II] reappeared to the NNW. By $\phi = 1.122$, the [Fe III] structure reappeared as in the previous early phase ($\phi = 0.213$) of the high-ionization portion of the cycle.

3.3 Variations with position angle and phase

We have demonstrated that, at PA = -28° , the extended structures of the [Fe III] and [Fe II] lines undergo major changes across periastron, but little changed across the spectroscopic high state. Now, we examine the available observations to map variations of the extended structures with PA.

Much happens as η Car B approaches η Car A. The orbital velocity of η Car B become comparable to the primary wind leading to wind structures being overtaken by η Car B (Nielsen et al. 2007a). The low-ionization primary wind wraps around the binary system, leading to trapping of the far-UV radiation in much denser, interior regions and the disappearance of the lower density, high-ionization forbidden lines. Fortunately, the bulk of the observations across the maximum was focused on the late high state beginning in early 2002, increasing in frequency at the beginning of the 2003.5 low state.

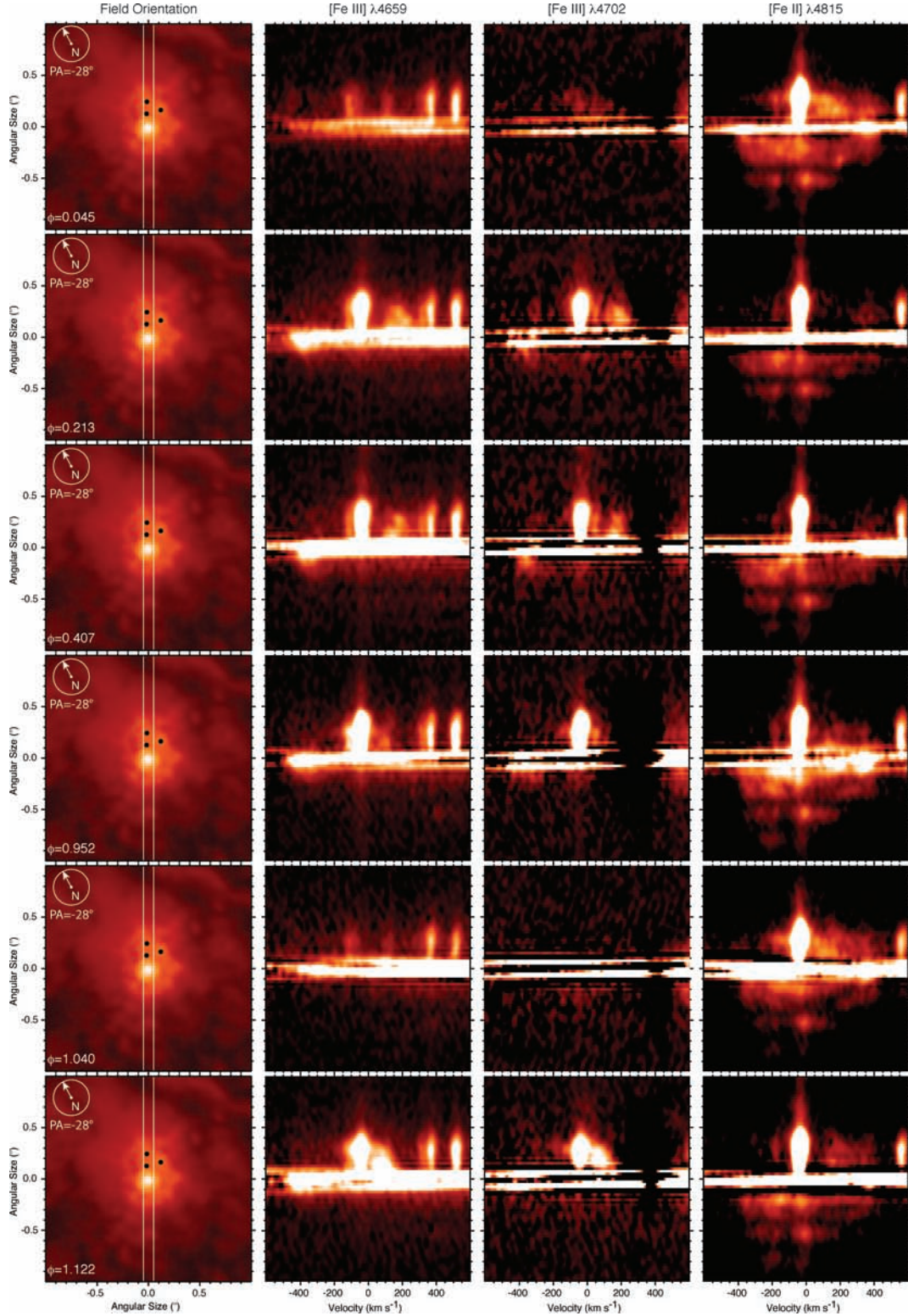


Figure 11. Spectro-images with $PA = -28^\circ$ for six phases, ϕ . This and subsequent figures will follow the convention: far left column – central 2×2 arcsec² field of η Car and ejecta, rotated to place – in the vertical – the superimposed 2-arcsec portion of the *HST*/STIS 52×0.1 arcsec² aperture. Spectro-images extending ± 600 km s⁻¹ centred on [Fe III] $\lambda 4659$ (centre right column), [Fe III] $\lambda 4702$ (centre right column), and [Fe II] $\lambda 4815$ (far right column).

Spectro-images tracing the line variations with PA and phase are reproduced in Figs 12–13. Fig. 12 focuses on changes with PA leading up to the periastron event. Fig. 13 follows the changes across the periastron passage.

Narrow-line emission in [Fe III] at -40 km s⁻¹ persists between $PA = -82^\circ$ and $+22^\circ$ (Fig. 12, rows 1–4), but is absent by $PA = +27^\circ$ (row 5). The far-UV radiation from η Car B excites low-velocity ejecta in directions from W through N to NNE. The

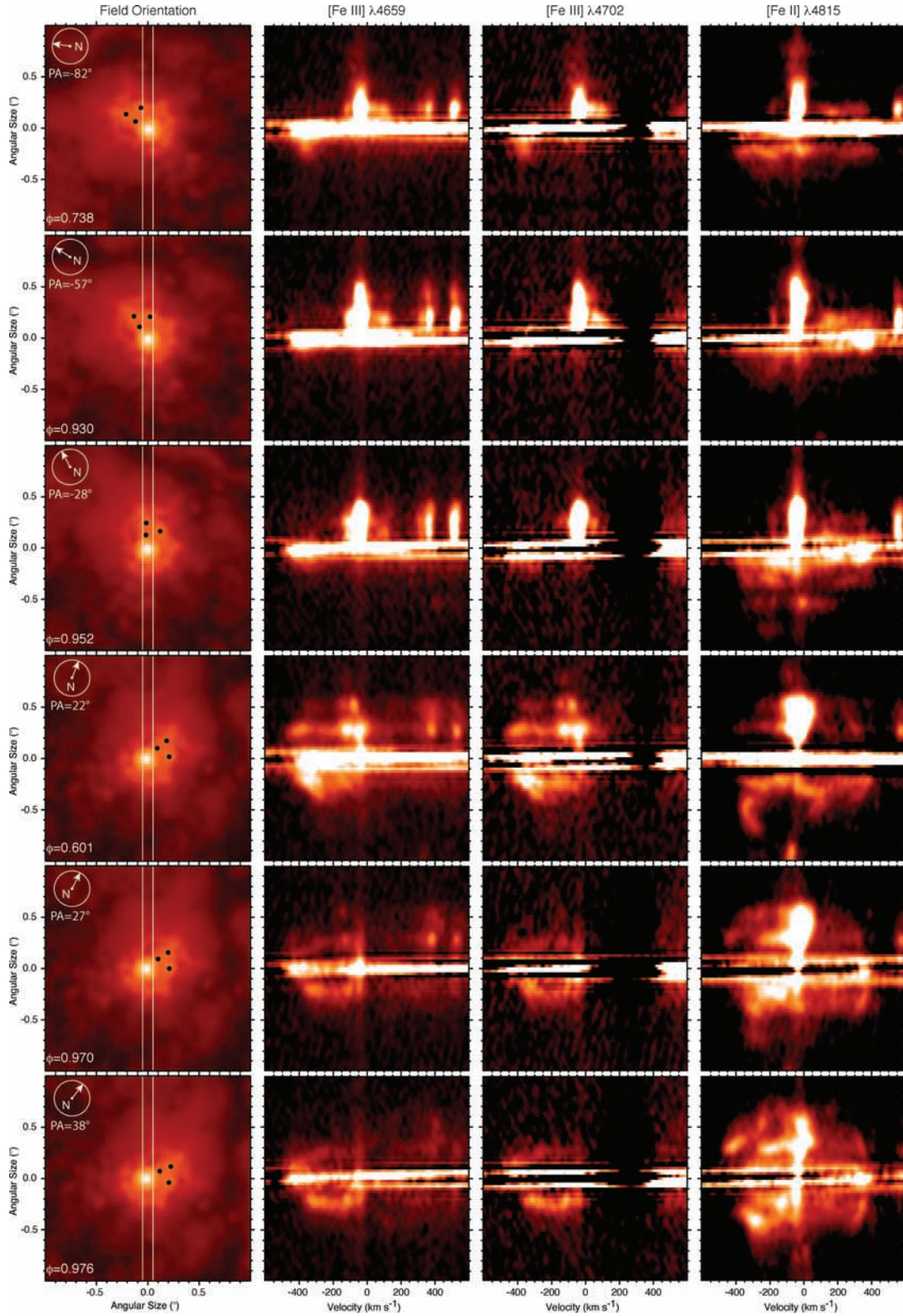


Figure 12. Variations of ionization with PA and ϕ . Here, PA changes dominate approaching periastron. The PA ranges from -82° to $+38^\circ$ and ϕ from 0.738 to 0.978 with the exception of row 4, recorded just after apastron, $\phi = 0.601$, included to compare changes with phase, $\phi = 0.946$ and 0.970.

narrow [Fe II] line emission tracks throughout these directions and beyond to PA = $+38^\circ$ (row 6). The narrow [Fe III] line emission is present a week before the X-ray drop (Fig. 13, rows 1 through 3). Ground-based monitoring by Damineli et al. (2008) shows it is

absent about four days after the X-ray drop. In contrast, the narrow [Fe II] line emission remains throughout the spectral low state.

The broad forbidden line profiles, as seen from the ground, resolve into complex spatial structures that change both with PA and

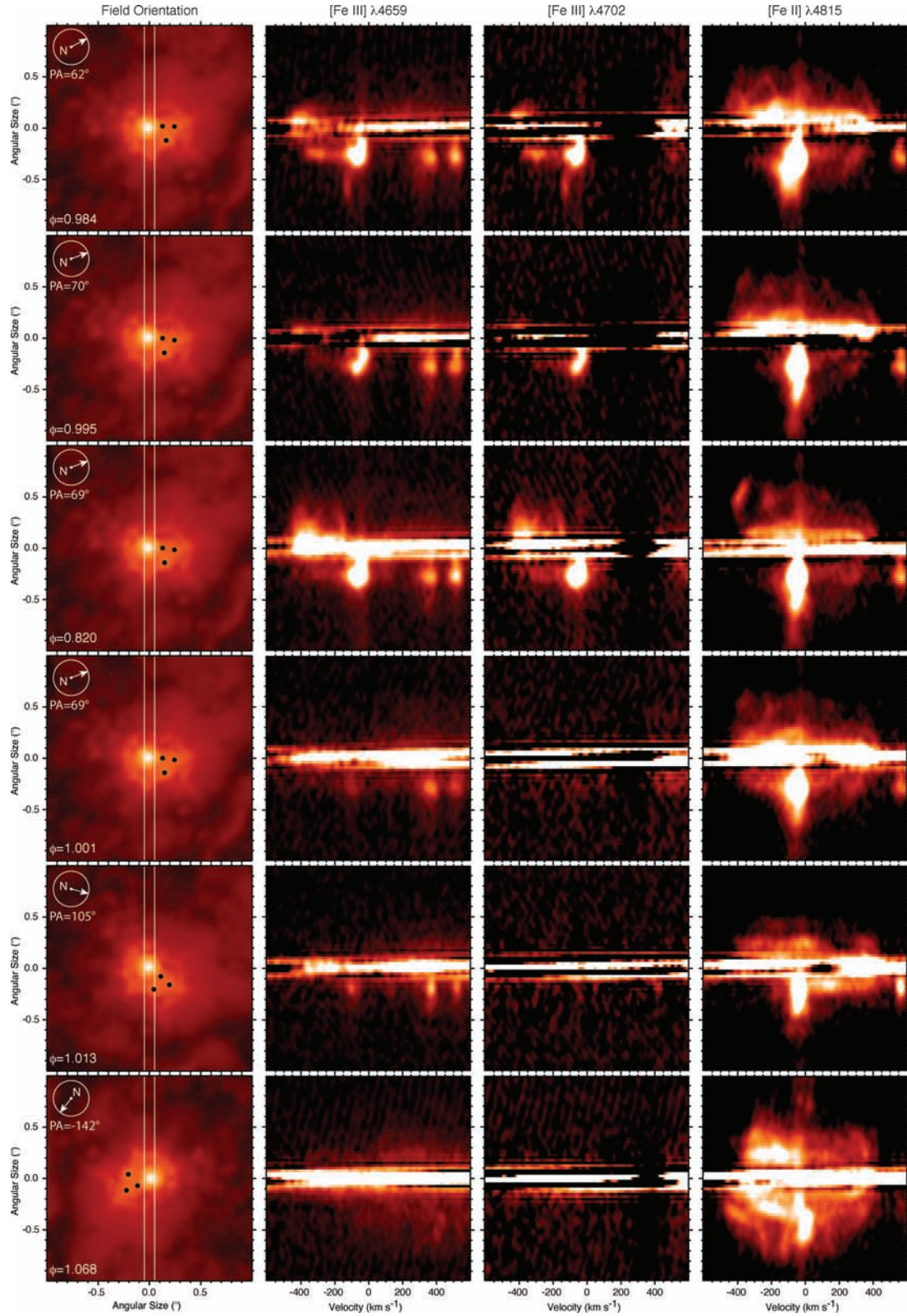


Figure 13. Variations of ionization with PA and ϕ continued. The focus is on changes across periastron so phase increases from $\phi = 0.984$ to 1.068 with the exception of row 3. The spectro-images in row 3 were 1 year before periastron at the same PA as the spectro-images in row 4, which were recorded one week after the X-ray drop. The two spectro-images in rows 2 and 4, recorded one week before and one week after the X-ray drop, demonstrate the abrupt disappearance of the high-ionization emission.

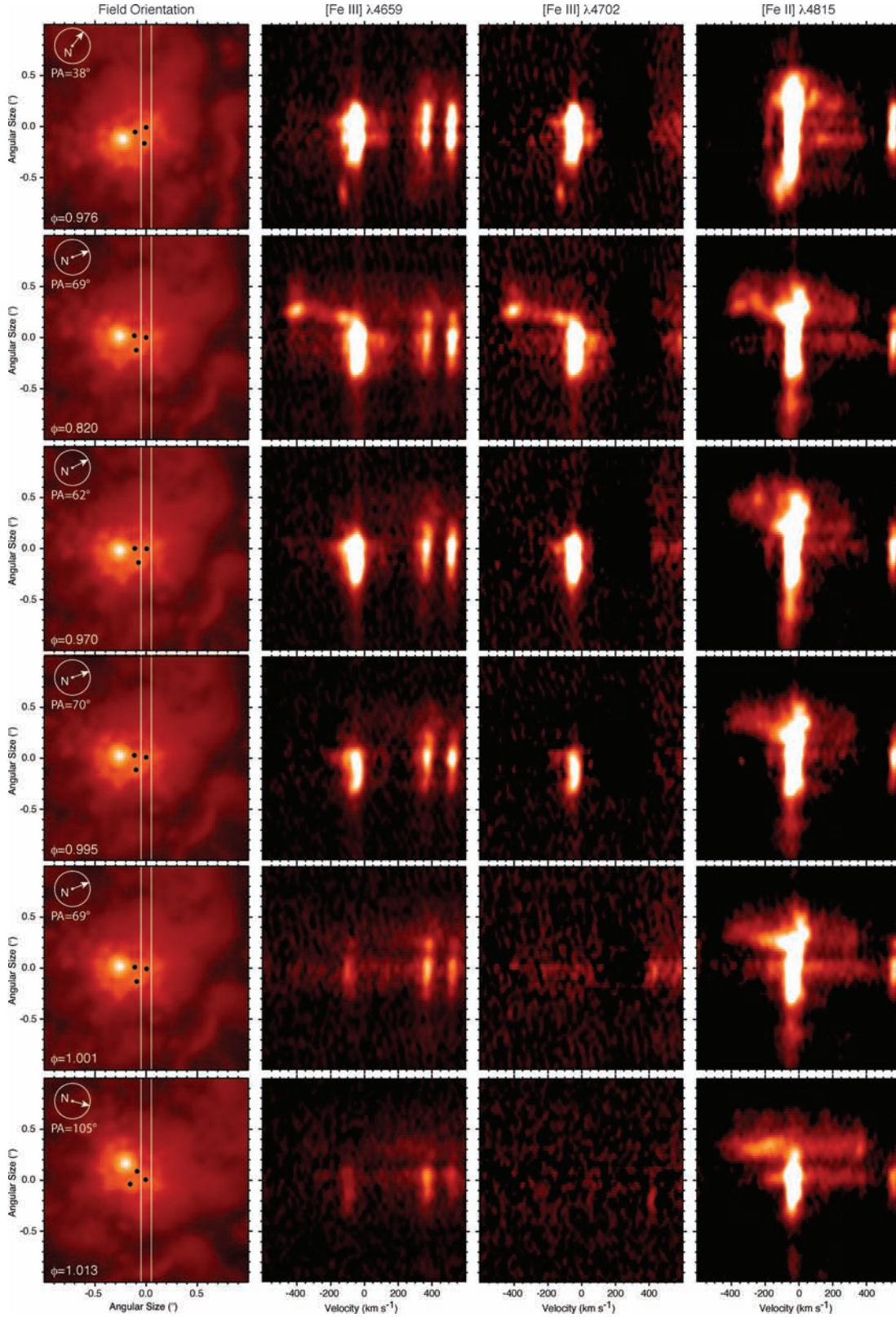


Figure 14. Weigelt D variations with ϕ and PA. Six observations, in parallel with those of η Car, were centred on Weigelt D to monitor changes across the spectroscopic low state. Both high- and low-ionization, spatially and velocity-resolved emission extends well beyond Weigelt D. A high-ionization, very high velocity structure appears connected to Weigelt D 1 year before the spectroscopic minimum (row 2, $\phi = 0.820$), but disappears well before the X-ray drop (row 3, $\phi = 0.970$). The high-ionization emission of Weigelt D fades before the X-ray drop and is completely absent during the low state. The [Fe II] emission appears to be further from η Car than the [Fe III] emission.

phase. Below, we describe the ionization changes by seen in spatial and velocity distribution.

(i) PA = -82° to -28° , Fig. 12 (rows 1–3).

The [Fe III] emission is similar to that observed for high-ionization states at constant PA = -28° (Fig. 11). A velocity and spatially resolved loop extends from -40 to $+200$ km s $^{-1}$ and 0.25 arcsec W to NNW. Weak emission extends from -300 to -500 km s $^{-1}$ and 0.2 arcsec E to SSE.

The [Fe II] emission changes notably especially from PA = -57° , $\phi = 0.930$ to PA = -28° , $\phi = 0.952$ (rows 2 and 3). The emission extends W to NW from 0 to -400 km s $^{-1}$ out to 0.3 arcsec, especially at PA = -57° , but fades at PA = -28° . SE to SSE, the emission extends ± 400 km s $^{-1}$, but only to about 0.25 arcsec at PA = -57° . At PA = -28° , the emission reaches beyond 0.7 arcsec.

(ii) PA = $+22^\circ$ to 38° , Fig. 12 (rows 4–6).

In this range of PAs, the [Fe III] emission structure is quite different compared to that seen with PA = -82° to -28° . The emission extends from -40 to -500 km s $^{-1}$ out to 0.5 arcsec NE and SW from the core position. The PA = $+22^\circ$, $\phi = 0.601$ observations (row 4) shows three narrow components with velocities of -80 , -140 and -350 km s $^{-1}$ located 0.5 arcsec NNE from the stellar position. The rest of the [Fe II] emission is best described as a ring extending in velocity from -40 to -500 km s $^{-1}$ and 0.3 arcsec NE and SW from the core.

The [Fe II] extended emission is different between PA = $+22^\circ$, $\phi = 0.601$ (row 4) and PA = $+27^\circ$, $\phi = 0.970$ (row 5). Given such a small change in PA, but a major change in phase, these spectro-images indicate a significant change in the [Fe II] emission between late apastron ($\phi = 0.601$) and just before periastron. The outer shell of the extended primary wind is brighter. A hook seen at -350 km s $^{-1}$ extended to 0.7 arcsec SW becomes much fainter and more diffuse than near apastron.

Both low- and high-ionization structures are quite similar as seen at PA = $+27^\circ$, $\phi = 0.970$ and PA = $+38^\circ$, $\phi = 0.976$, indicating that the spatial and ionization structures change slowly in the late high-ionization stage.

(iii) PA = $+62^\circ$ to -142° ($=38^\circ$ – 180°), Fig. 13.

The [Fe III] ring emission is less well defined at PA = $+62^\circ$, $\phi = 0.984$ (row 1), weeks before the drop in X-ray flux. By PA = $+70^\circ$, $\phi = 0.995$ (row 2), less than a week before the X-ray drop, the [Fe III] emission has dropped considerably in intensity and shows as a bright little hook to the WSW. For comparison, the spectro-images recorded at PA = $+69^\circ$, $\phi = 0.820$ (row 3) show the bright [Fe III] structure a year earlier. This position is repeated at PA = $+69^\circ$, $\phi = 1.001$ (row 4), a week after the X-ray drop, demonstrating the absence of the broad component of the high-ionization lines. Followup observations at PA = $+105^\circ$, $\phi = 1.013$ and PA = $+142^\circ$ confirm the complete absence of [Fe III] deep in the spectroscopic low state.

The [Fe II] emission varies considerably with PA and phase across the periastron event. Comparison of PA = $+62^\circ$, $\phi = 0.984$ (row 1) to PA = $+70^\circ$, $\phi = 0.995$ (row 2) demonstrates that small PA changes near periastron lead to differences in the outer [Fe II] emission that are more notable than between the two [Fe II] spectro-images at PA = $+69^\circ$, $\phi = 0.820$ (row 3) and PA = $+70^\circ$, $\phi = 0.995$ (row 2) recorded 1 year apart. Most of the emission is about the same intensity in both spectro-images. However, the spectro-image taken at PA = $+69^\circ$, $\phi = 1.001$ (row 4) indicates a filled-in core and much less extended emission.

The [Fe II] emission is not symmetrical at any phase. During the low state, at PA = -142° the [Fe II] extends to 0.5 arcsec SW and 0.8 arcsec NE the stellar position while at PA = $+105^\circ$ the broad component is confined to ± 0.3 arcsec (E and W) relative to the stellar position. Comparing PA = -142° during the minimum to PA = $+38^\circ$ ($=-142^\circ + 180^\circ$) during the late high state indicates that the outer portions of the [Fe II] emission are mirror images. The increased brightness of the interior [Fe II] emission at PA = -142° , $\phi = 1.068$ appears to correlate with the [Fe III] emission at PA = $+38^\circ$, $\phi = 0.976$ (Fig. 12, row 6) consistent with a drop in ionization.

3.4 Changes in Weigelt D with phase

The Weigelt condensations, being slowly moving, denser clumps of gas, effectively serve as probes in the wind structure. Here, we describe variations from the high state to the low state and their location within. Fig. 14 presents spectro-images from observations specifically centred on Weigelt D, offset by 0.252 arcsec at PA = -22° (NNW).

The spectro-images recorded at PA = $+38^\circ$, $\phi = 0.976$ (Fig. 14, row 1) are dominated by bright, narrow emission lines of [Fe III] and [Fe II], centred on Weigelt D. Much additional spatial and velocity structure is present, largely due to intersections of outer portions of the wind interaction regions. The [Fe II] emission includes an almost continuous loop that reaches from Weigelt D to 0.4 arcsec NE at -40 km s $^{-1}$ then back towards Weigelt D at -200 km s $^{-1}$. The loop brightens about 0.5 arcsec SW and comes back to -40 km s $^{-1}$ extending through Weigelt C. Striations in [Fe II] extend to $+400$ km s $^{-1}$ at the position of Weigelt D. Little of the loop shows up in [Fe III]. However, a bright, slightly extended feature, located 0.7 arcsec W of η Car, appears on the ring of [Fe II] at -125 km s $^{-1}$. This emission does not correlate with any emission seen by Weigelt & Ebersberger (1986), or any structure in the *HST*/ACS images.

Four spectra of Weigelt D were recorded near PA = $+69^\circ$ at different phases. The spectro-images at $\phi = 0.820$ (Fig. 14, row 2) show a blue-shifted arc that starts ENE of Weigelt D and shifts to -500 km s $^{-1}$ at a position 0.4 arcsec NE of η Car. A [Fe II] emission is complementary, shifting to -400 km s $^{-1}$ and extending beyond the [Fe III] emission to 0.7 arcsec NE of η Car. 1 year later just before the spectroscopic low state, three observations were obtained (Fig. 14, rows 3–5). The extended, high-velocity component of [Fe III] is not present at the phases near periastron ($\phi = 0.970, 0.995$ and 1.001). The outer [Fe II] emission remains but is significantly shifted and more diffuse. Both peculiar high-velocity components noted in Fig. 14 (rows 1, 2) appear to be related to structures in the wind interface regions that encounter brief illuminations by the far-UV radiation of η Car B.

Two observations were obtained during the low state: PA = $+69^\circ$, $\phi = 1.001$ (Fig. 14, row 5) and PA = $+105^\circ$, $\phi = 1.013$ (Fig. 14, row 6). Both show only weak [Fe III] narrow-line emission from Weigelt D. The [Fe II] broad-line emission extends from -200 to 400 km s $^{-1}$ at the position of Weigelt D, similar to that seen just after the X-ray drop, and stronger than the year earlier.

3.4.1 Temperature and density estimates

Many additional lines of doubly ionized species have been identified, but most are fainter or blended with nearby bright lines. However, the spatial and velocity structure can be used to separate contributions of the doubly ionized emission lines. The [S III],

$\lambda\lambda 9533$, 9071 and 6313 , are well isolated. Their intensity ratio, a function of n_e and T_e (Osterbrock & Ferland 2006), leads to $n_e = 10^7 \text{ cm}^{-3}$ and $T_e = 10^4 \text{ K}$, consistent with that derived for an averaged spectrum of Weigelt D and B (Verner et al. 2005). The line fluxes of the -350 km s^{-1} component seen at PA = $+69^\circ$, $\phi = 0.820$ (Fig. 14, row 2) lead to a slightly lower density and temperature. The flux ratio for the short extended structure to the NW of the -350 km s^{-1} feature, relatively bright in [S III] $\lambda 9533$, 9071 , but very faint in [S III] $\lambda 6303$, indicates a drop in T_e and/or n_e . We note that the unidentified line in the spectrum of η Car at 6307 \AA (Martin et al. 2006a) is the -500 km s^{-1} emission component of [S III] $\lambda 6313$.

3.4.2 Increase in brightness

Martin et al. (2006b) demonstrated that the apparent brightening of η Car from 2002 to 2006 was constrained to the central 1 arcsec while the Homunculus did not brighten substantially, and that the Weigelt condensations did not brighten proportionately. Their review of observations back to the initial speckle observations (Weigelt & Ebersberger 1986) suggests that the Weigelt condensations were comparable in brightness to η Car in the 1980s, but have brightened less rapidly. They noted that the relative change in brightness in η Car versus the Weigelt condensations implies that the spatial scale of change in extinction is of the order of 0.1 arcsec, or the distance from Weigelt B to η Car.

The change in brightness of Weigelt B and D can be constrained further with *HST*/STIS spectroscopy. Observations in 1998 March and 2003 September were obtained one full period apart at PA = -28° and 152° ($= -28^\circ + 180^\circ$) deep in the spectroscopic low state (Fig. 15). The extracted spectra of Weigelt B and D are identical both in excitation and in flux. In contrast, the spectrum of η Car brightened by about one stellar magnitude in the visible. The net effect, as viewed by ground-based spectroscopy, would be that the narrow emission line contribution by the Weigelt condensations appears to be fading. As demonstrated by *HST*/STIS flux-calibrated spectra, η Car is brightening but the Weigelt condensations are not. This explains the apparent fading of the Weigelt condensations relative to η Car from their initial discovery in the 1980s (Weigelt & Ebersberger 1986) to even more recent speckle interferometry measures (Weigelt, private communication).

At the position of the Weigelt condensations, a continuous ‘stellar’ spectrum is visible. The light source is η Car. The starlight, scattered by dust within the condensations (Figs 15 and 16), presents

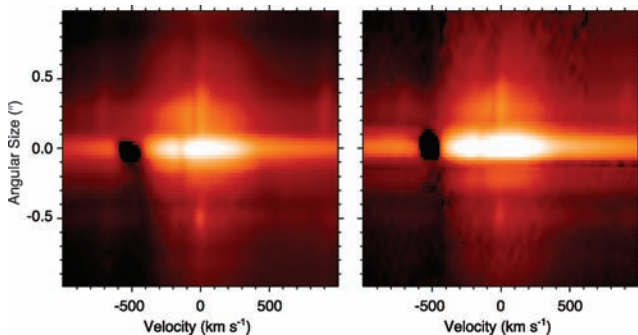


Figure 15. Comparison of spectro-images of H I $\lambda 6564$ recorded in the spectroscopic low states of 1998.3 ($\phi = 0.045$) and 2003.5 ($\phi = 1.040$). The spectrum from 2003 September was recorded with the slit rotated 180° from the -28° PA of 1998 March. For convenience of the reader, the spectro-image has been mirror imaged. The spectral extractions are plotted in Fig. 16.

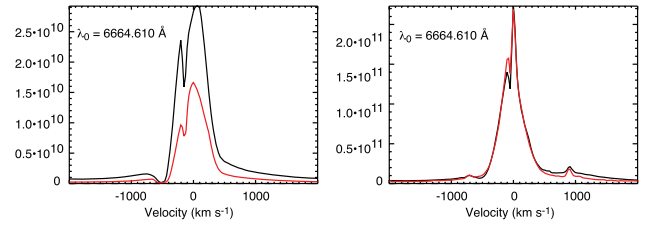


Figure 16. Velocity plots of H I $\lambda 6564$ for (left-hand panel) η Car and (right-hand panel) Weigelt B and D combined. The red tracings were extracted from the 1998 March ($\phi = 0.045$) and the black tracings were from 2003 September ($\phi = 1.040$), one period later. The peak of the H α emission, and the continuum, has increased two fold for η Car while the H α profile scattered by Weigelt B and D is nearly identical.

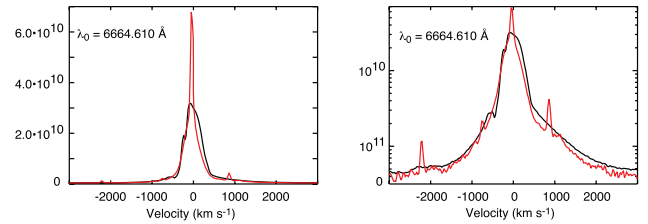


Figure 17. H I $\lambda 6564$ profiles of η Car and Weigelt BD at $\phi = 0.403$. While P-Cygni absorption is very weak in the spectrum of η Car, it is not present in the scattered spectrum off Weigelt B and D. Note: spectrum of Weigelt BD had been scaled to match the continuum level of η Car.

the star spectrum as seen by the Weigelt condensations. The velocity plots of η Car (left-hand panel) show that H α increased twofold while the scattered starlight off of Weigelt B and D (not easily separable at 6564 \AA due to wavelength-dependent diffraction limits of *HST*) did not change. Moreover, the wind profiles, seen directly (compared to wind profiles seen scattered off of the condensations), are dramatically different. The very strong P-Cygni absorption seen in line of sight at periastron (Fig. 16) is quite weak in the starlight scattered by the Weigelt condensations. Such is not the case for the scattered starlight seen in the extended wind structure on the opposite side of η Car from Weigelt D. Indeed, during the broad high state, the velocity profiles scattered off of Weigelt B and D show negligible P-Cygni absorption. Allowing for the nebular narrow-line H α emission, the electron-scattered wind profile is seen by the Weigelt condensations are fairly symmetrical (see Fig. 17).

Difference images of the central region (Smith et al. 2004a), recorded before and after the X-ray drop in 2003.5, show a near-UV excess to the SW of η Car along with a darkening to the NE. After the event, the reverse is seen, namely a smaller excess to the NE and a large darkening to the SW. The plane of the dusty skirt, located between the two lobes of the Homunculus, projects in a line from the SW to the NE. A simple explanation of the changes is that η Car B passed from the SW to the NE during the low state. We thus have two significant clues about the orbit of η Car: the cavity driven by η Car B lies on the near side of η Car A for most of the orbit, passing beyond η Car A during periastron, and η Car B approaches η Car A from the SW and recedes from the NE.

3.4.3 Location of the Weigelt condensations

The Weigelt condensations are excited by far-UV from η Car B (Verner et al. 2005). Here, we showed that, during the high state, there is no P Cygni absorption in the H I $\lambda 6564$ wind emission scattered by the dust associated with Weigelt D. The hydrogen column

lying between η Car B and Weigelt D must be fully ionized. Moreover, Nielsen et al. (2007a) observed near-UV Fe II P Cygni profiles scattered off of Weigelt D. While the central core in our line of sight brightened over one period, Weigelt D did not, demonstrating that the far-UV radiation impinging upon Weigelt D did not increase. Likewise, the Homunculus has not brightened substantially, indicating that the overall radiation on the surrounding ejecta has not increased. Likely, the properties of dust or the quantity of dust have changed uniquely in our line of sight. Given the fitful changes in stellar flux seen over the recent decade, is this evidence that the non-uniform wind interaction region in our line of sight contributes to random apparent flux variations?

The velocity of Weigelt D (-47 km s^{-1} ; Nielsen et al. 2007a) is blue shifted with respect to the system velocity of η Car (-8 km s^{-1} ; Smith 2004). Weigelt D is located in the direction of the observer with respect to η Car. Moreover, the highly ionized forbidden emission arising from the wind interaction zone is blue shifted. The emerging picture is that the cavity, driven by η Car B, lies on this side of η Car. Within this cavity, the Weigelt condensations are slow-moving probes.

4 A WORKING MODEL

4.1 Developing a working model

Features in the spectra reveal at least three environments that can be distinguished by their excitation and velocity profile: the Weigelt condensations, the wind interaction structures and the outer wind. The Weigelt condensations (high-density, slow-moving ejecta from the 1890 event) contribute bright, narrow emission lines with width $< 50 \text{ km s}^{-1}$ centred at $\approx -40 \text{ km s}^{-1}$ (Figs 11–14). In contrast, the forbidden wind line emission originates from a collection of features from the fossil, interacting winds of η Car A and η Car B ejected over the past decade. This material moves much faster, up to the terminal speed of η Car A's wind ($\sim 500 \text{ km s}^{-1}$). Forbidden emission line features manifest themselves in the form of arcs/rings, as seen in [Fe III] (Figs 11–13, middle two columns) or as more complex outer loops ([Fe II]; Figs 11–13, far-right column).

A complete model of the η Car system will need to include the Weigelt condensations, that act as probes in the winds, but this is beyond the scope of the current paper. Instead, we focus on the current wind and the wind interaction regions. The three-dimensional smoothed particle hydrodynamic (SPH) simulations of Okazaki et al. (2008) proved successful in modelling η Car's X-ray light curve. We use a model by Okazaki expanded in distance to understand the *HST*/STIS observations. Fig. 18 shows the results of a three-dimensional SPH simulation of the winds on a scale comparable to the innermost and the outermost regions of the system, $\sim 1500 \text{ au}$ or 0.67 arcsec . The methodology, as well as the stellar wind, and the orbital parameters are the same as in Okazaki et al. (2008), with the exception that the outer simulation boundary is set to $100a$ ($1a \equiv 1 \text{ semimajor axis} = 15.4 \text{ au}$). Note that in the inner $15a$ the surface formed by the colliding winds is well approximated by an axisymmetric cone with a constant half-opening angle $\alpha = 65^\circ$, in good agreement with the analytic momentum balance analysis of Canto, Raga & Wilkin (1996). On a larger scale, the model becomes more complex: the extended wind–wind interface develops a tear-drop shape in the orbital (xy) plane (outlined in yellow in Fig. 18, upper-left panel). During the periastron passage, the wind of η Car B becomes embedded in η Car A's wind, while at apastron the massive wind of η Car A flows outwards unimpeded. This creates a dense shell of material that continues outwards as

η Car B completes its periastron passage and the inner regions regain their near-conical shape (Fig. 18, upper-right panel).

4.2 A cone model for forbidden line emission

Some of the prominent features in the spectro-images are the blue-shifted arc/ring-like structures observed in the high-ionization, forbidden wind lines of Figs 5–9 and Fig. 12 (middle two columns). For simplicity, we assume that the colliding wind interface can be modelled via an axisymmetric cone, or paraboloid, similar to the insets of Fig. 18. We adopt the line of sight derived by Okazaki et al. (2008), for which the orbital plane is tilted 45° away from the observer and rotated by $\Phi = 27^\circ$ in the prograde direction from the apastron side of the semimajor axis (in this case, counterclockwise in the skirt plane). This corresponds to an argument of periapsis, $\omega \equiv 270^\circ - \Phi = 243^\circ$.

The highly ionized, forbidden lines are strongest in a gas with densities near n_c , above which electron collisions depopulate the metastable level before radiative de-excitation can occur. Typical critical densities for these transitions (Table 3) range from 5×10^5 to $3 \times 10^7 \text{ cm}^{-3}$. If the high ionization lines are signatures of the wind interaction region, then the maximum critical radius, r_c , at which an individual line forms in the cone wall is

$$\frac{r_c}{10a} = \left[\frac{1.91 \times 10^7}{n_c} \frac{\dot{M}_{-3}}{v_{500}} f_\alpha \right]^{1/2}, \quad (1)$$

where \dot{M}_{-3} is the mass-loss rate in units of $10^{-3} M_\odot \text{ yr}^{-1}$, v_{500} is the wind terminal speed in units of 500 km s^{-1} and f_α is the compression factor for the material in the shock-cone wall. For a cone with half-opening angle α and a wall of angular width $\delta\alpha$, the compression factor compared to a spherically symmetric wind is $f_\alpha \equiv (1 - \cos\alpha)/(\sin\alpha \delta\alpha)$. For $\alpha = 65^\circ$ and $\delta\alpha = 3^\circ$, $f_\alpha = 10$. This enhancement comes from η Car A's wind material, that normally would be within the cavity carved out by the wind of η Car B, being pushed to the walls of the cone.

The colliding wind surface from the current wind interaction generates very dense structure within $15a$ or 0.1 arcsec , which is comparable to the CCD detector spatial resolution of *HST*/STIS. However, highly ionized, forbidden emission seen by *HST*/STIS extends out to 0.4 arcsec , indicating far-UV excitation of much more extended, lower density structures consistent with wind structure created during the previous period. For the following model discussion, we continue with an axisymmetric paraboloid with the knowledge that both the SPH model and the observations indicate distortion in the orbital plane. More accurate modelling is deferred to a later paper as additional modelling and possibly future observations are required.

Table 4 lists the estimated radii of emission rings for forbidden lines of various critical densities. To better match the spatial scales of the observed structures, these estimates use the mass-loss rate, $\dot{M} = 10^{-3} M_\odot \text{ yr}^{-1}$, from Hillier et al. (2001, 2006), instead of the factor of 4 smaller mass-loss rate used by Okazaki et al. (2008) for the SPH simulations.

To reproduce the blue-shifted, high-ionization emission, we consider the line-of-sight velocity of material in the dense walls of the inner shock cone. The walls are composed primarily of η Car A wind material flowing at the dominant wind speed of $\sim 500 \text{ km s}^{-1}$. The projected line-of-sight velocity along the cone surface is shown in Fig. 19. The top illustration is of an axial-symmetric cone directly calculated using the geometric orientations discussed above. The bottom illustration is the projected velocity structure from the walls of the wind interaction region directly from the inner $10a$ of a

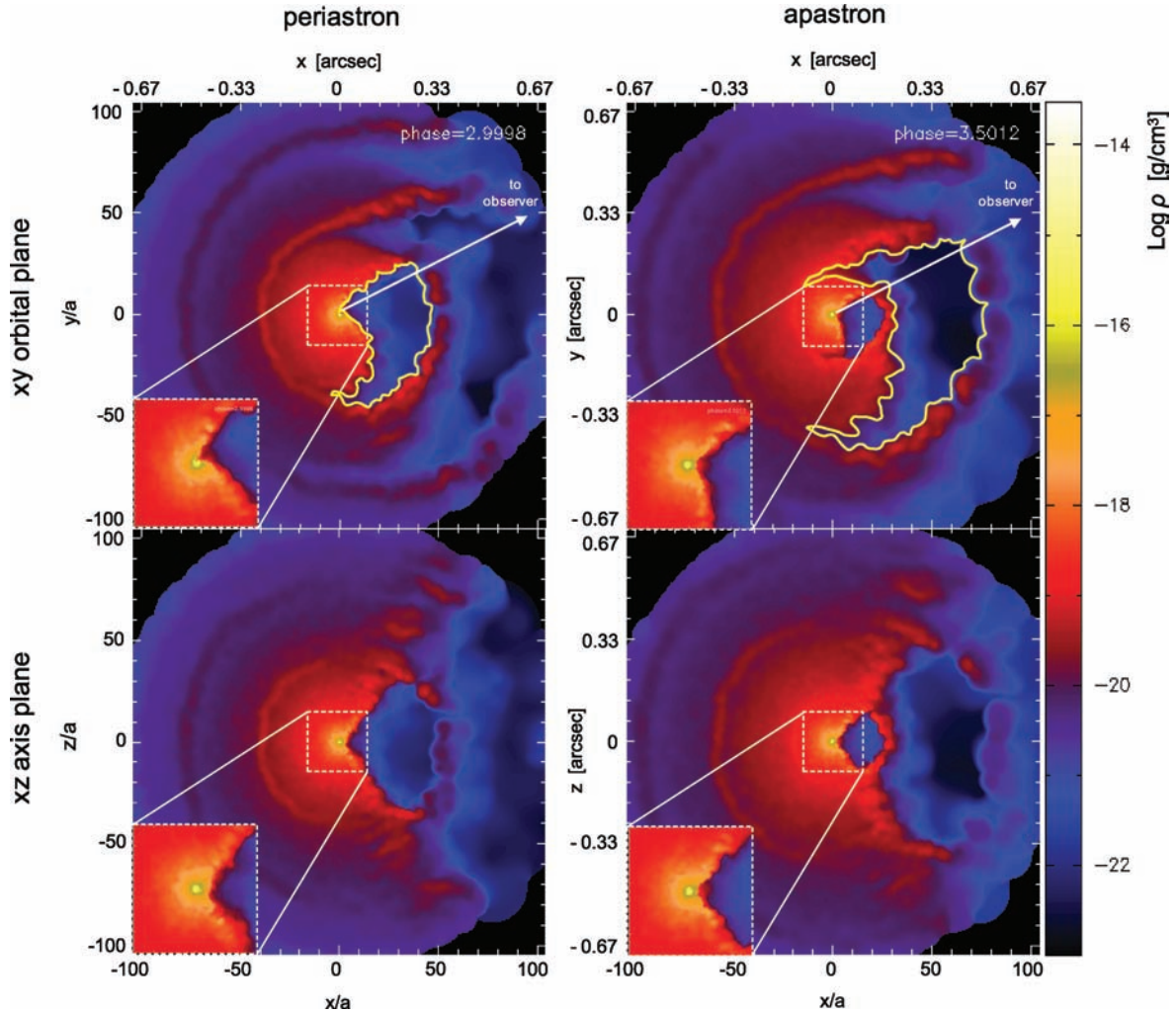


Figure 18. Snapshots of the three-dimensional SPH simulation of the wind interaction in η Car at periastron (left-hand panels, $\phi = 1$) and apastron (right-hand panels, $\phi = 0.5$). The colour scale shows the density measured in the xy orbital plane (top panels) and the xz perpendicular plane containing the orbital and major axes (bottom panels). The outer simulation boundary is at $100a$ (corresponding to 0.67 arcsec) while the lower-left insets show the inner $15a$ (0.1 arcsec). The tear-drop shaped wind cavities (in yellow) define the outer extended wind.

Table 4. Modelled parameters.

Wind line	n_c (cm^{-3})	r_c^a (arcsec)	d^b (arcsec)
[Ne III] $\lambda 3868$	1×10^7	0.29	0.35
[Ar III] $\lambda 7137$	4×10^6	0.46	0.50
[S III] $\lambda 9533$	5×10^5	1.30	0.50
[Fe III] $\lambda 4659$	$\sim 10^7$	0.29	0.60
[N II] $\lambda 5756$	3×10^7	0.17	0.55

^aCalculated value.

^bObserved ring diameter.

three-dimensional SPH simulation. For both illustrations, the back side of the paraboloid is lengthened and red shifted since it is tilted away from the observer, while the near side is foreshortened and blue shifted. The density range is chosen to show material confined to the walls of the interaction surface. The similarity between the top and bottom panels of Fig. 19 shows that the analytic model captures the essential features of the wind interaction within $10a$ of the binary system.

4.3 Application to two specific slit positions

We assume that the axisymmetric cone, or paraboloidal, model applies to the outer wind interaction region – that left over from the previous period and extending out to $\sim 100a$, ~ 0.67 arcsec, in Fig. 18. We now use this model to reproduce specific features seen in the slit spectra of [Fe III]. As an example, we focus on spectra for orbital phase $\phi = 0.976$ at PA = $+38^\circ$ (Fig. 8) and for $\phi = 0.952$ at PA = -28° (Fig. 11, row 4, middle two columns).

4.3.1 The orbit orientation

To compare the spectro-images with this model, we must establish the absolute orientation of the shock cone. A key result of Okazaki et al. (2008) is that the η Car X-ray light curve is best fitted when the line of sight passes within the wind cavity formed by η Car B. However, their model is degenerate with respect to the absolute orientation of the binary orbit. The shock-cone axis of symmetry can have any orientation within a conical surface spun around our line of sight. To remove this degeneracy, it is commonly assumed that the orbital plane lies in the equatorial skirt, with the orbital angular momentum axis pointing along the symmetry axis of the

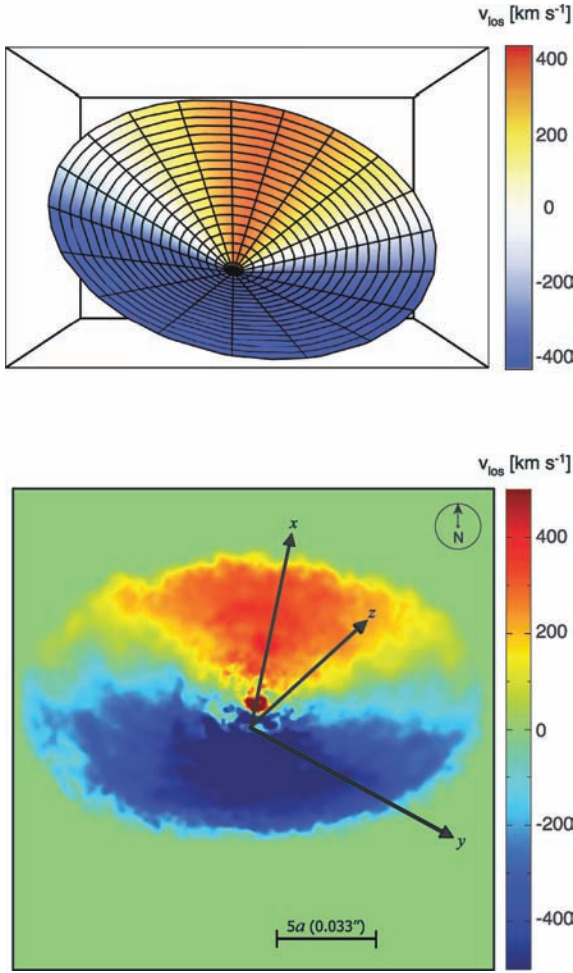


Figure 19. Velocity-encoded wind interaction surfaces. Colour indicates line-of-sight velocity of material towards (or away from) the observer. Top panel: the projected analytic three-dimensional shock cone oriented at the same observer's line-of-sight as the best fit from Okazaki et al. (2008). Note that the cone in this image is concave, open towards the observer. Bottom panel: the wind interaction region directly from a three-dimensional SPH model extending out to $10a$. In this image, the x -axis is the semimajor axis of the orbit (pointing to apastron), while the y -axis is the semiminor axis (the xy -plane is the orbital plane). The z -axis (orbital angular momentum axis aligned to the Homunculus axis of symmetry) is perpendicular to the orbital plane, which is tilted 45° away from the observer and rotated by $\phi = 27^\circ$.

Homunculus. This defines the major axis (in direction of apastron) and the axis of the paraboloid such that their projections point to the NNW on the sky as depicted in Fig. 19.

However, when the shock-cone model with this orientation is used to derive slit spectra, the results for the two cases with $PA = +38^\circ$ and -28° are quite different from observations. Synthetic spectro-images did not show the symmetrical blue-shifted emission as seen in spectro-images with PAs ranging from 20° to 40° . Likewise, the red-shifted component was not pronounced for -28° . To reproduce observed spectro-images, the axis of the cone had to be shifted from east to west. We tried new orientations of the paraboloid in the prograde direction along the orbital plane at 10° intervals up to 50° . Better fits to the two spectral images were obtained with a paraboloidal model whose axis is rotated by a prograde 30° , moving on the sky from NNW to NW. Fig. 20 illustrates such a rotated model, with the superimposed STIS apertures.

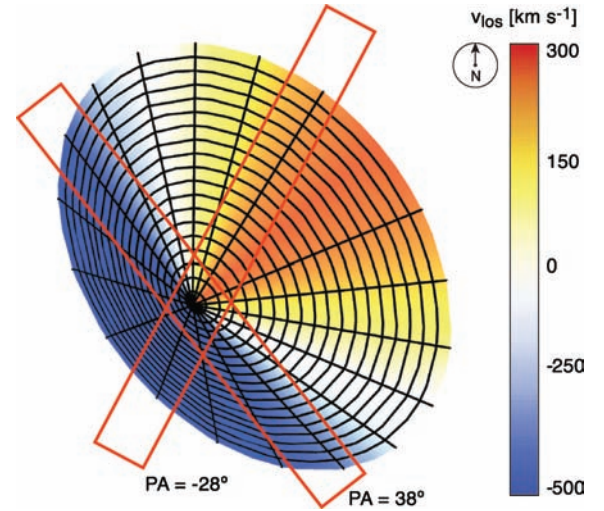


Figure 20. Velocity-encoded surface of the three-dimensional analytic shock cone used to model the ring-like structures observed in the high-ionization forbidden line of [Fe III]. The STIS aperture, with width = 0.1 arcsec (230 au, $\approx 15a$) is superimposed at PAs of $+38^\circ$ and -28° .

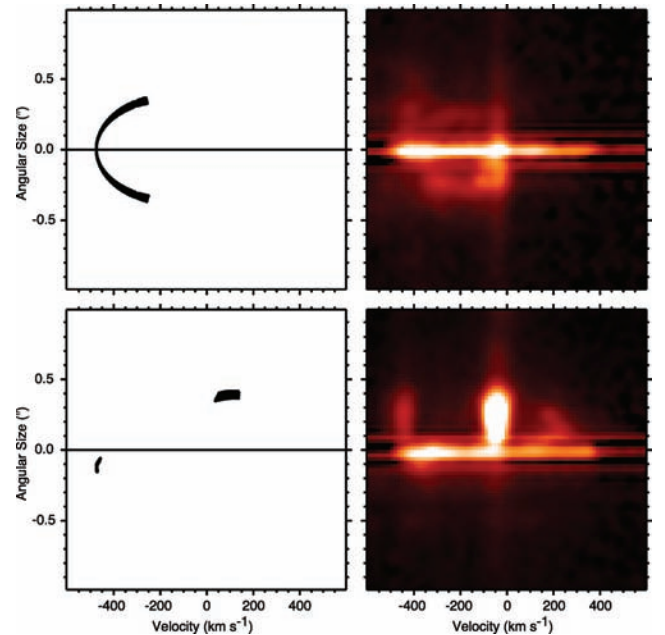


Figure 21. Comparison of synthetic and observed [Fe III] spectro-images. Top-left panel: synthetic spectro-image derived from the analytic shock cone depicted in Fig. 20 with the *HST*/STIS aperture positioned at 38° . Top-right panel: observed spectro-image at $\phi = 0.976$ and $PA = +38^\circ$. Bottom-left panel: synthetic spectro-image derived from the analytic shock cone depicted in Fig. 20 with the *HST*/STIS aperture positioned at -28° . Top-right panel: observed spectro-image at $\phi = 0.952$ and $PA = -28^\circ$.

We created each synthetic spectro-image by isolating regions of the cone that have a density within ~ 25 per cent of the critical density, $n_c = 10^7 \text{ cm}^{-3}$. We identified the projected line-of-sight velocity for the presumed Doppler-shifted line emission from this region, and plotted the implied emission as a function of projected position along the slit. Fig. 21 shows the results. The qualitative agreement with the observed spectro-image, particularly the arc in Fig. 21 (top panels), illustrates the potential for this simplified

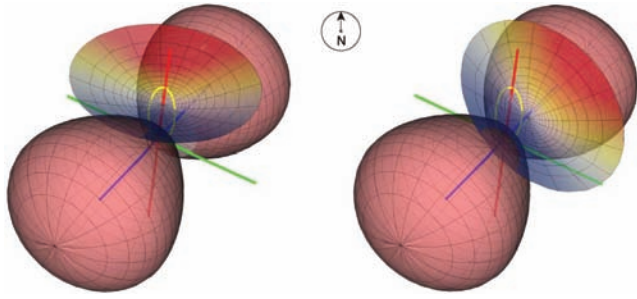


Figure 22. Illustration showing the relationship of the binary orbit (yellow) and the shock cone relative to the Homunculus. In both the left- and right-hand figures, the orbital plane is depicted as in the skirt plane with the orbital axis (blue) aligned to the Homunculus axis of symmetry. On the left is an axisymmetric paraboloid as it would appear at apastron if the cone axis were aligned to the orbit major axis (red). On the right is the paraboloid with the conical axis shifted by 30° prograde in the orbital plane = Homunculus skirt. (the cone size is arbitrarily increased for illustrative purpose. North is up.)

approach to model the *HST*/STIS data. However, the discrepancy in predicting the red-shifted component, in Fig. 21 (bottom panels), is significant. It suggests that the paraboloidal structure is not axisymmetric, but is compressed in the polar directions. This may be due to η Car A's latitudinal-dependent wind as noted by Smith et al. (2003). Compared to line-of-sight H α P-Cygni absorption, higher wind velocities are seen in scattered light from the centre of the foreground Homunculus lobe. More detailed modelling and mapping of the wind structure is necessary to substantiate the distortions of the cone.

The paraboloidal model that best describes the observed spatial/velocity structure of the highly ionized forbidden lines has its axis of symmetry rotated about 30° along the orbital plane, or the plane of the skirt. The orbital angular momentum axis remains aligned with the Homunculus axis of symmetry. As a visual aid to the reader, we include Fig. 22 illustrating the shift of the paraboloidal cone relative to the geometries of the Homunculus and the X-ray derived orbit, with the binary orbital axis aligned to the Homunculus axis of symmetry. Note that the paraboloid size is greatly expanded for ease of viewing. This result, which combines visible and X-ray observations with a three-dimensional model, provides structure to the system, but requires confirmation by further study and more complete models. This simplistic cone model is an illustration of how dynamical models can be exploited to analyse the *HST* observations.

5 DISCUSSION

Many papers have been published on the orbit orientation of the massive binary. The majority accept an orbit in which η Car B is on the far side of η Car A across periastron (Damineli 1996; Corcoran et al. 2001; Pittard & Corcoran 2002; Corcoran 2005; Akashi, Soker & Behar 2006; Hamaguchi et al. 2007; Nielsen et al. 2007a; Henley et al. 2008; Okazaki et al. 2008). However, Falceta-Gonçalves, Jatenco-Pereira & Abraham (2005), Abraham et al. (2005), Abraham & Falceta-Gonçalves (2007) and Kashi & Soker (2007) place η Car B is on the near side of η Car A at periastron. Both Ishibashi (2001) and Smith et al. (2004a) concluded that the periastron orientation is at quadrature. Parkin et al. (2009) submitted a paper describing independent three-dimensional dynamical modelling of the wind–wind collision fitted to the *RXTE* light

curve. They affirmed that η Car B is on the far side of η Car A at periastron.

The models of Okazaki et al. (2008) and Parkin et al. (2009), when applied to the *RXTE* light curve, provide ambiguous solutions: a class of orbit orientations consistent with the orbital angular momentum axis tilted at about 45° from the sky plane. They do not confine the PA on the sky as, in three-dimensional space, the models do not confine the orbital rotational axis to align with the major axis of the Homunculus. That is assumed. Both models show that the wind interaction in the orbital plane exhibits a characteristic asymmetry in the wind structure due to the highly eccentric orbit of the binary system and the very different wind momenta of the primary and secondary. As demonstrated in Fig. 18 and by Parkin et al. (2009), the cavity formed by η Car B's wind shifts in a prograde direction along the orbital plane, an effective rotation of 30° along the orbital plane. Spatially resolved observations are necessary to determine the alignment or misalignment of the orbital angular momentum axis with the Homunculus, or correspondingly, the alignment of the orbital plane with the Homunculus skirt.

The available spectro-images coarsely bound the orientation of the orbital plane to the skirt plane. The highly ionized emission is completely blue shifted for orientations from PA = $+27^\circ$ to $+38^\circ$, but partially red shifted for all other angles, most notably at PA = -28° (see Figs 11–13). As shown in Fig. 20, the velocity structures seen in the spectro-images correspond to a paraboloid whose axis projects on the sky at PA $\approx -25^\circ$. Moreover, the Weigelt condensations, located in the NW quadrant, and the weaker ionized structures (Figs 11–13) η Car are located in a region bounded by PAs from $+38^\circ$ to -82° in a clockwise direction. We see no narrow-line emission in the complimentary region. The far-UV radiation ionizes portions of the Homunculus skirt on the near side, but not the far side of η Car. The small H II region associable with η Car is located to the NW, in the same general direction as the Weigelt condensations (Duncan & White 2003). With a maximum size of 3–4 arcsec, the ionized hydrogen emission follows the highly excited emission lines, shrinking and expanding in concert with the periodic maxima. Velocity measures of both the Weigelt condensations and the H II emission are likewise consistent with the structures lying in the skirt of the Homunculus. The strontium filament (Zethson 2001; Hartman et al. 2004) located at the outer boundary of the H II region also has blue-shifted velocity corresponding to the near side of the Homunculus skirt, and the He I $\lambda 10830$ emission traced by Teodoro et al. (2008) extends in the same general direction defining photo-excited skirt structure extending well beyond the projected structure of the north-west lobe. We conclude that the hot η Car B (1) spends most of the orbit on the near side of η Car A and (2) across the broad high state maintains the highly ionized structure in the NW portion of the Homunculus skirt. The projected angular size of this ionized structure is bounded by the complex wind. Some highly ionized emission is seen in the Little Homunculus (Ishibashi et al. 2003) above and below the ionized skirt regions but does not extend to the inner boundary of the Homunculus.

By virtue of the blue-shifted, highly ionized emission, apastron must be on the near side of η Car A and periastron on the far side. We again note that the imagery of Smith et al. (2004b) supports excess UV emission on the SW side of η Car just before periastron and to the NE just after. This is consistent with the hot secondary, η Car B, pre-periastron, approaching η Car A from the SW and post-periastron receding to the NE.

Immersion from the SW and emersion to the NE, with apastron on the near side, suggest a clockwise motion of η Car B on the sky

relative to η Car A. The presence of ionized material to the NW only in the skirt plane supports the orbital plane being closely aligned with the skirt plane. Hence, the orbital angular momentum axis is in near alignment to the major axis of the Homunculus.

We again examine both the model in this paper and that in Parkin et al. (2009). The dimensional size of the high-ionization emission extends out to 0.35 to 0.60 arcsec (800 to 1400 au), well beyond the distances that the winds travel in a current cycle, but comparable to the distances traversed by wind features in the previous cycle and with densities in the wind interaction regions comparable to that which would lead to emission of [Fe III], etc. [the model of Parkin et al. (2009) has a finite cut-off around 1000 au leading to the model wind collision region structure artificially thinning out in the outer regions relevant to the spectro-images describe herein. In this paper, we extended the model of Okazaki et al. (2008) to $100a$, corresponding to 0.67 arcsec (1500 au).]

Both models show an extended cavity in the orbital plane advanced in the prograde direction by about 30° . Our vantage point appears to be such that, while the X-ray derived orientation of the major axis is towards N, the prograde cavity is shifted to the NW, thus leading to the observed high-ionization lines originating from the orbital plane with a symmetry at angles around $+22^\circ$ to $+38^\circ$. Not all of the extended cavity will show the highly ionized forbidden emission as far-UV radiation from η Car B must have a direct path to impinge upon gas with densities close to the critical density for a specific emission line. Much of the outer cavity can be shielded by denser, less ionized material between the inner and the outer wind-blown cavities.

With the available spectro-images, we are unable to further constrain the orbit. However, the orbit orientation can be further constrained and the shape of the cavity can be better defined by improved models that predict the extended wind structure at specific phases in the orbital period and by complete mappings of the highly ionized emission lines with *HST*/STIS, or instruments with comparable, or better, spatial and spectral resolutions, at critical phases. The models are in further development. Further observations await repair of *HST*/STIS and future observatories with imaging spectrographs capable of providing spatial maps of density across this spatially resolved structure. Such will lead to greatly increased understanding of massive winds.

6 SUMMARY

The *HST*/STIS spatially resolved, moderate-resolution spectra of η Car have resolved extended, velocity-shifted emission from (1) high ionization (Fe^{2+} , Ne^{2+} , S^{2+} and Ar^{2+}) and (2) low ionization (Fe^+). Spectro-images were extracted of selected lines of these ions, plus permitted lines of H, He and Fe^+ . Permitted emission of H, He and Fe^+ originates primarily from the binary, not resolved by *HST*/STIS. By contrast, the forbidden line emission is spatially and velocity-resolved into arcs and rings that define outer structures of the massive interacting winds. The high-ionization, forbidden emission is primarily blue shifted up to -500 km s^{-1} relative to the system, but the low-ionization, forbidden emission extends to $\pm 500 \text{ km s}^{-1}$. An empirical paraboloidal model fitted to the *HST*/STIS data is consistent with an outer wind interaction structure lying in the Homunculus skirt plane. Its axis of symmetry projects on the sky in the same direction as the H II region mapped by Duncan & White (2003), the strontium filament and the He I emission traced by Teodoro et al. (2008). However, the paraboloid that fits the structure seen in high-ionization lines is rotated along the Homunculus skirt plane by $\approx 30^\circ$ from the major axis of the binary system derived

from the X-ray light-curve (Okazaki et al. 2008; Parkin et al. 2009). This difference in orientation is caused by the high eccentricity and the periastron event. Much of the primary wind gas flows in the direction of apastron during the low state, leading to the distortion of the cavity carved out by η Car B, shifting the conical axis in a prograde direction in the orbital plane.

Further modelling using both SPH and other hydrodynamic codes with radiative transfer will be necessary to fully understand the spatial structure and variations with phase, but this analysis does illustrate the importance of using slit spectra in determining the geometric and physical properties of the binary system. Improved models in turn will be tested with current, and hopefully future, *HST*/STIS and other high-spatial-resolution mappings of the high- and low-ionization forbidden lines of interest.

ACKNOWLEDGMENTS

We acknowledge the many, very fruitful discussions with Gerd Weigelt, Jose Groh, Vincent Icke and Augusto Damineli. Their interest and excitement have encouraged us to study the *HST*/STIS spectra of η Car in considerable detail and to build this preliminary model. Much remains to be done both in modelling and followup observations, but that is the exciting future!

The *HST* observations were accomplished through STIS GTO, *HST* GO and *HST* η Car Treasury Team programmes. All analysis was done using STIS IDL software tools on data available through the *HST* η Car Treasury archive. Don Lindler provided very useful display tools for generating the spectro-images. TIM and CMPR were supported through the NASA Graduate Student Research Programme.

REFERENCES

- Abraham Z., Falceta-Gonçalves D., 2007, MNRAS, 378, 309
- Abraham Z., Falceta-Gonçalves D., Dominici T., Caproni A., Jatenco-Pereira V., 2005, MNRAS, 364, 922
- Akashi M., Soker N., Behar E., 2006, ApJ, 644, 451
- Appenzeller I., Oestreicher R., 1988, AJ, 95, 45
- Canto J., Raga A. C., Wilkin F. P., 1996, ApJ, 469, 729
- Corcoran M. F., 2005, AJ, 129, 2018
- Corcoran M. F., Ishibashi K., Swank J. H., Petre R., 2001, ApJ, 547, 1034
- Damineli A., 1996, ApJ, 460, L49
- Damineli A. et al., 2008, MNRAS, 384, 1649
- Davidson K. et al., 2005, AJ, 129, 900
- Duncan R. A., White S. M., 2003, MNRAS, 338, 425
- Falceta-Gonçalves D., Jatenco-Pereira V., Abraham Z., 2005, MNRAS, 357, 895
- Hamaguchi K. et al., 2007, ApJ, 663, 522
- Hartman H., Gull T., Johansson S., Smith N., HST Eta Carinae Treasury Project Team, 2004, A&A, 419, 215
- Henley D. B., Corcoran M. F., Pittard J. M., Stevens I. R., Hamaguchi K., Gull T. R., 2008, ApJ, 680, 705
- Hillier D. J., 1988, ApJ, 327, 822
- Hillier D. J., Davidson K., Ishibashi K., Gull T., 2001, ApJ, 553, 837
- Hillier D. J. et al., 2006, ApJ, 642, 1098
- Iping R. C., Sonneborn G., Gull T. R., Massa D. L., Hillier D. J., 2005, ApJ, 633, L37
- Ishibashi K., 2001, in Gull T. R., Johansson S., Davidson K., eds, ASP Conf. Ser. 242, Eta Carinae and Other Mysterious Stars: The Hidden Opportunities of Emission Spectroscopy, Searching for Physically Acceptable Parameters for Eta Carinae's Companion. Astron Soc. Pac., San Francisco, p. 53
- Ishibashi K. et al., 2003, AJ, 125, 3222

- Kashi A., Soker N., 2007, *New Astron.*, 12, 590
- Kimble R. A. et al., 1998, *ApJ*, 492, L83
- Martin J. C., Davidson K., Hamann F., Stahl O., Weis K., 2006a, *PASP*, 118, 697
- Martin J. C., Davidson K., Humphreys R. M., Hillier D. J., Ishibashi K., 2006b, *ApJ*, 640, 474
- Nielsen K. E., Gull T. R., Vieira Kober G., 2005, *ApJS*, 157, 138
- Nielsen K. E., Ivarsson S., Gull T. R., 2007a, *ApJS*, 168, 289
- Nielsen K. E., Corcoran M. F., Gull T. R., Hillier D. J., Hamaguchi K., Ivarsson S., Lindler D. J., 2007b, *ApJ*, 660, 669
- Nielsen K. E., Kober G. V., Weis K., Gull T. R., Stahl O., Bomans D. J., 2009, *ApJS*, 181, 473
- Okazaki A. T., Owocki S. P., Russell C. M. P., Corcoran M. F., 2008, *MNRAS*, 388, L39
- Osterbrock D. E., Ferland G. J., 2006, *Astrophysics of Gaseous Nebulae and Active Galactic Nuclei*, 2nd edn. University Science Books, CA
- Parkin E. R., Pittard J. M., Corcoran M. F., Hamaguchi K., Stevens I. R., 2009, *MNRAS*, in press (doi:10.1111/j.1365-2966.2009.14857.x)
- Pittard J. M., Corcoran M. F., 2002, *A&A*, 383, 636
- Smith N., 2004, *MNRAS*, 351, L15
- Smith N., 2006, *ApJ*, 644, 1151
- Smith N., Davidson K., Gull T. R., Ishibashi K., Hillier D. J., 2003, *ApJ*, 586, 432
- Smith N., Morse J. A., Collins N. R., Gull T. R., 2004a, *ApJ*, 610, L105
- Smith N. et al., 2004b, *ApJ*, 605, 405
- Stahl O., Weis K., Bomans D. J., Davidson K., Gull T. R., Humphreys R. M., 2005, *A&A*, 435, 303
- Steiner J. E., Damineli A., 2004, *ApJ*, 612, L133
- Teodoro M., Damineli A., Sharp R. G., Groh J. H., Barbosa C. L., 2008, *MNRAS*, 387, 564
- Verner E. M., Gull T. R., Bruhweiler F., Johansson S., Ishibashi K., Davidson K., 2002, *ApJ*, 581, 1154
- Verner E. M., Bruhweiler F., Gull T. R., 2005, *ApJ*, 624, 973
- Weigelt G., Ebersberger J., 1986, *A&A*, 163, L5
- Weigelt G. et al., 2007, *A&A*, 464, 87
- Whitelock P. A., Feast M. W., Koen C., Roberts G., Carter B. S., 1994, *MNRAS*, 270, 364
- Woodgate B. E. et al., 1998, *PASP*, 110, 1183
- Zanella R., Wolf B., Stahl O., 1984, *A&A*, 137, 79
- Zethson T., 2001, PhD thesis, Lund Univ.

This paper has been typeset from a \TeX/L\AA\TeX file prepared by the author.